University of Alberta

INTERNAL WAVE TUNNELLING

by

Geoffrey L. Brown ©

A thesis submitted to the Faculty of Graduate Studies and Research in
partial fulfillment of the requirements for the degree of

Master of Science

Department of Earth and Atmospheric Sciences

Edmonton, Alberta
Spring 2008

Library and
Archives Canada

Published Heritage
Branch

395 Wellington Street
Ottawa ON K1A 0N4
Canada

Bibliothèque et
Archives Canada

Direction du
Patrimoine de l'édition

395, rue Wellington
Ottawa ON K1A 0N4
Canada

Your file Votre référence
ISBN: 978-0-494-45782-5
Our file Notre référence
ISBN: 978-0-494-45782-5

NOTICE:
The author has granted a non-exclusive license allowing Library and Archives Canada to reproduce, publish, archive, preserve, conserve, communicate to the public by telecommunication or on the Internet, loan, distribute and sell theses worldwide, for commercial or non-commercial purposes, in microform, paper, electronic and/or any other formats.

The author retains copyright ownership and moral rights in this thesis. Neither the thesis nor substantial extracts from it may be printed or otherwise reproduced without the author's permission.

AVIS:
L'auteur a accordé une licence non exclusive permettant à la Bibliothèque et Archives Canada de reproduire, publier, archiver, sauvegarder, conserver, transmettre au public par télécommunication ou par l'Internet, prêter, distribuer et vendre des thèses partout dans le monde, à des fins commerciales ou autres, sur support microforme, papier, électronique et/ou autres formats.

L'auteur conserve la propriété du droit d'auteur et des droits moraux qui protège cette thèse. Ni la thèse ni des extraits substantiels de celle-ci ne doivent être imprimés ou autrement reproduits sans son autorisation.

In compliance with the Canadian Privacy Act some supporting forms may have been removed from this thesis.

While these forms may be included in the document page count, their removal does not represent any loss of content from the thesis.

Conformément à la loi canadienne sur la protection de la vie privée, quelques formulaires secondaires ont été enlevés de cette thèse.

Bien que ces formulaires aient inclus dans la pagination, il n'y aura aucun contenu manquant.

Canada

Abstract

We examine the transmission of internal gravity waves through non-uniformly stratified fluid using piecewise-linear theory and fully nonlinear numerical simulations. Transmission coefficients are measured using the ratio of the flux of transmitted to incident pseudoenergy, T. An analytic prediction of T is found for waves tunnelling through a piecewise-linear shear flow in which the fluid is unstratified over the depth of the shear and uniformly stratified elsewere. In weak shear, transmission across critical layers, where the phase speed of waves matches the flow speed, is possible if the background density profile is continuous. For a discontinuous background density profile no transmission occurs through critical layers, however, transmission values increase at other phase speeds. Numerical simulations of wavepackets show little dependence of transmission values on wavepacket extent and a significant increase in transmission values for larger initial wave amplitudes.

Acknowledgements

First and foremost, I would like to thank my supervisors, Bruce Sutherland and Andy Bush, for giving me the opportunity to further my education. Their guidance and direction were invaluable in shaping this research and the knowledge I have gained from them will serve me well in the future. I would especially like to thank Bruce who was the creative force behind this project. This work is an extension of his own and I appreciate the opportunity to be a part of it.

I would also like to thank my family and friends who have supported me along the way. Especially, my parents, Kevin and Patti, who fostered a love of math and science early on and were there to nurture my passion as it grew. My girlfriend, Melisa, has helped me through the stressful times when the work seemed too difficult to handle on my own. I could count on her to do the daily chores when I was too busy. My research group and other colleagues, especially Josh Nault and James Munroe, were an excellent sounding board and provided many insights through discussions. The time spent with those around me here at the U of A made my time more meaningful and enjoyable.

I want to thank the following agencies that have provided funding that made this work possible: the Natural Sciences and Engineering Research Council of Canada (NSERC), the Canadian Foundation for Climate and Atmospheric Sciences (CFCAS), and the Alberta Ingenuity Studentship program.

Finally, I would like to thank my committee members for their time, comments, and constructive criticism on my thesis.

Table of Contents

List of Tables

List of Figures

Chapter 1

Introduction

Internal gravity waves play an important role in redistributing energy and momentum throughout Earth's oceans and atmosphere. Driven by buoyancy forces, internal gravity waves propagate both vertically and horizontally through stratified fluids transporting energy and momentum away from the original source. Stratified fluids are fluids in which the background density, $\bar{\rho}(z)$, varies with height. In stably stratified fluids the background density decreases monotonically with height so that dense fluid lies below less dense fluid. As waves propagate they eventually may become unstable, so that heavy fluid is lifted above lighter fluid, and break, depositing energy and momentum to the background flow leading to increased drag and mixing. There are many examples of this process occurring in nature. Polzin et al. (1997) and Ledwell et al. (2000) have shown the structure and intensity of the abyssal ocean circulation is, in part, controlled by internal waves generated over oceanic ridges. As waves propagate upward into the ocean they break and provide a significant source of the energy required for ocean mixing, which consequently redistributes heat and modulates Earth's climate. In another ocean study, Skyllingstad and Denbo (1994) examined the growth of internal gravity waves due to surface wind stress in the equatorial ocean and concluded these waves have a large effect on the equatorial undercurrent. Internal waves play an important role in the atmosphere as well. McFarlane (1987) and McLandress (1998) have shown that breaking internal waves in the atmosphere are an important factor in determining the structure of the mean winds and thus atmospheric circulation patterns. They conclude effective parameterizations of gravity wave drag are necessary for accurate numerical weather predictions and global climate models.

In this work the propagation of internal waves over small scales is studied. The internal waves studied here are restricted to a Boussinesq fluid in two dimensions. The Boussinesq approximation is applicable to internal waves which propagate over distances in which the background density changes by only a small fraction of itself. This is a good approximation for the ocean in which the density changes by less than 10% between the ocean floor and surface. In the atmosphere the approximation is applicable for waves traversing distances much less than the density scale height, defined as $H_\rho = -\bar{\rho}/\frac{\mathrm{d}\bar{\rho}}{\mathrm{d}z}$. Typically, $H_\rho \sim 8$ km in the atmosphere.

Internal waves propagate with a frequency no larger than the buoyancy frequency, N, which under the Boussinesq approximation is defined as

$$N^2(z) = -\frac{g}{\rho_0}\frac{\mathrm{d}\bar{\rho}}{\mathrm{d}z}. \tag{1.1}$$

Here g is the gravitational acceleration and ρ_0 is a characteristic density of the background. The buoyancy frequency, sometimes called the Brunt-Väisälä frequency, is the natural frequency of vertical oscillations in a stratified fluid. Provided the stratification and background horizontal flow, $\bar{U}$, are steady and independent of x, the absolute wave frequency, ω, and horizontal wavenumber, k, of internal waves remain constant as waves propagate. However, the relative (or 'Doppler-shifted') frequency,

$$\bar{\Omega}(z) = \omega - k\bar{U}(z), \tag{1.2}$$

is a function of the background properties and can vary with height. In order for waves to propagate through a stratified fluid the relative frequency must remain less than the buoyancy frequency (*i.e.* $\bar{\Omega} < N$) at all heights. If $\bar{\Omega} > N$ waves are said to be 'evanescent disturbances' that decay exponentially away from such heights. Trajectories of internal wave propagation and calculations of energy and momentum transport are typically performed using 'ray tracing' techniques (Lighthill, 1978; Broutman et al., 2004). These techniques apply the WKB approximation which requires a scale separation that assumes the vertical scale of variations of the background fields, $\bar{U}(z)$ and $N(z)$, are large compared to the vertical wavelength of waves. Applying simple heuristics based on ray theory, small-amplitude waves are predicted to reflect from a height z_r (a reflection level) where $\bar{\Omega} = N$ and asymptotically approach a height z_c (a critical level) where $\bar{\Omega} = 0$ (Bretherton, 1966). This research shows that when the scale separation is reversed so that the vertical wavelength of waves is on the order of, or larger than, the vertical scale of variations of the background, waves can indeed penetrate across reflection and critical levels. The circumstance, being analogous to electron tunnelling in quantum mechanics, is referred to here as 'internal wave tunnelling'.

Internal wave tunnelling between two ducts in the ocean has previously been described theoretically by Eckart (1961), who considered resonant energy transfer between different vertical modes of the main and seasonal thermocline in the ocean. The atmospheric counterpart to Eckart resonance was described by Fritts and Yuan (1989) who additionally considered the effects of Doppler-shifting winds. This work usefully describes the two-way periodic energy transfer between ducts by low-order modes; however, it cannot describe one-way tunnelling of small vertical-scale internal waves from one highly stratified region to another.

Unidirectional tunnelling was examined by Lindzen and Tung (1976), who studied the reflection and over-reflection of atmospheric internal gravity waves.

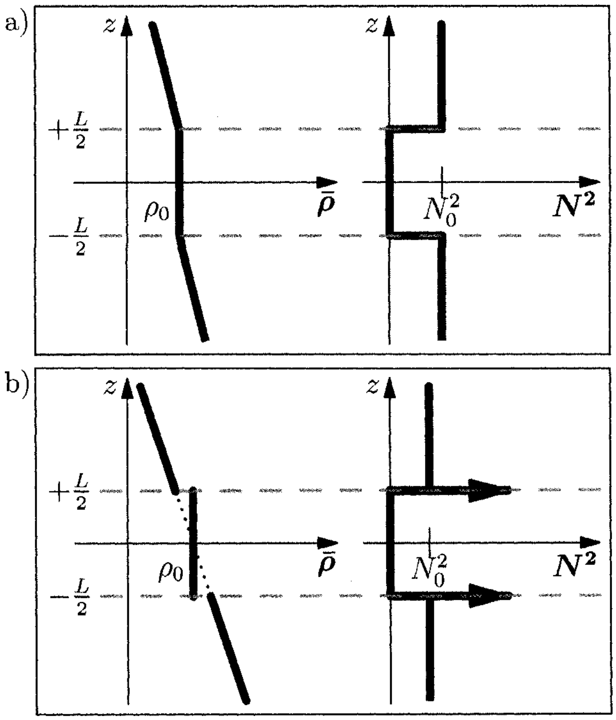

Figure 1.1: Background density (left) and squared buoyancy frequency (right) defined for a) an 'N^2-barrier' and b) a 'mixed-N^2' profile.

Their study was restricted to low-order mesoscale modes and so filtered non-hydrostatic waves with frequencies close to the buoyancy frequency. This work was continued by Wang and Lin (1999) who examined more general background velocity and density profiles.

An analytic theory for non-hydrostatic internal wave tunnelling through a weakly stratified fluid layer was derived by Sutherland and Yewchuk (2004). In particular they examined internal wave tunnelling through what they termed an 'N^2-barrier', which consisted of a continuously varying background density profile in three distinct layers. The outer two layers were uniformly stratified with buoyancy frequency N_0 while the inner layer had uniform density and thus a buoyancy frequency of zero, seen in Fig. 1.1a. Tunnelling through a N^2-barrier can be viewed as an idealization of several large-scale geophysical flows. In the atmosphere it is representative of waves tunnelling from the stratosphere, through an evanescent region in the mesosphere, to the ionosphere. In the ocean it is representative of waves tunnelling from the seasonal to the main thermocline. Defining the transmission coefficient as the ratio of transmitted to incident energy they found, in particular, that the maximum transmission across an N^2-barrier occurs for waves having frequency $\omega = N_0/\sqrt{2}$. They also studied tunnelling through a 'mixed-N^2' profile in which stratification was the same as in the N^2-barrier case except that it exhibited discontinuous density jumps on either flank of the unstratified region, seen in Fig. 1.1b. This circumstance was representative of a mixed layer caused by local mixing within an initially uniformly stratified fluid. They found that waves could transmit more effectively than through an N^2-barrier and that a transmission spike occurred when the vertically propagating waves interacted resonantly with interfacial waves on either flank of the shear layer.

1.1 Thesis Overview

In this thesis, the work of Sutherland and Yewchuk (2004) is extended to explore the additional effects upon tunnelling of background shear, compact wavepackets, and finite wave amplitudes.

In Chapter 2 the effect of a shear layer coinciding with an unstratified region is examined. Linear theory is used to develop the tools needed to predict analytically and to quantify internal wave transmission through shear layers.[1] The stability of a particular parallel shear flow is discussed in Section 2.4. The addition of shear makes the mixed-N^2 case of Section 2.5.2 in particular, more closely resemble a mixed layer in the ocean. The presence of shear may act as a source of local mixing that results in a uniform density region.

Chapter 3 uses numerical simulations to determine the effect amplitude has

---

[1] This work has been published by Brown and Sutherland (2007)

on transmission. Simulation stability criteria and time dependent transmission quantification methods are developed. The effect of compact wavepackets is also explored.

Chapter 4 provides a summary of significant findings and discusses how they may be applied in atmospheric and oceanic situations. In Appendix A the theory of internal gravity waves is developed. Beginning from the basic equations governing fluid motion, the fundamental equations and properties of internal waves under the assumptions relevant to this study are provided. It may be helpful for readers unfamiliar with internal gravity waves to begin with this material.

Chapter 2

Linear Tunnelling

2.1 Introduction

In this chapter the theoretical tools necessary to model and analyze the propagation of linear internal gravity waves in a Boussinesq fluid are developed. These tools are then used to predict analytically the transmission of internal waves through non-uniformly stratified fluid with vertically varying background shear.

In Section 2.2 the techniques used to solve the Taylor-Goldstein equation, which describes the motion of Boussinesq fluid in a non-uniform background, for piecewise linear profiles are presented. A method for quantifying the relative transmission of internal waves through specific background profiles using pseudoenergy is described in Section 2.3. The stability of a specific parallel shear flow is then examined in Section 2.4 and the transmission of internal waves through this flow is described in Section 2.5.

2.2 Governing Equation

In order to come up with an analytic prediction for internal wave transmission this portion of the study is restricted to small-amplitude disturbances in a Boussinesq fluid. The perturbation streamfunction associated with disturbances having horizontal wavenumber, k, and (absolute) frequency, ω, is

$$\psi(x,z,t) = \phi(z)e^{i(kx-\omega t)} + \text{c.c.}, \tag{2.1}$$

where the streamfunction amplitude, ϕ, satisfies the Taylor-Goldstein equation

$$\phi'' + m^2(z)\phi = 0 \tag{2.2}$$

where

$$m^2(z) = k^2\left(\frac{N^2}{\bar{\Omega}^2} + \frac{\bar{U}''}{k\bar{\Omega}} - 1\right). \tag{2.3}$$

In this formula $\bar{\Omega}$ is the relative frequency of waves given by (1.2). For a complete derivation of this equation see Sections A.1 and A.2. If m^2 is constant for all z in the domain, solutions are either exponential or sinusoidal functions (*i.e.* $\phi = Ae^{imz}$ is a solution if m^2 is positive). This occurs if N^2 is piecewise-constant and $\bar{U}$ is piecewise-linear such that N^2 is zero where $\bar{U}$ is variable.

A complete solution for ϕ is found by matching the functions determined over each piecewise-linear segment using conditions that require the vertical displacement and pressure to be continuous. This is done by requiring

$$\Delta\left[\frac{\phi}{\bar{\Omega}}\right] = 0 \tag{2.4a}$$

and

$$\Delta\left[\bar{\rho}\left(\bar{\Omega}\phi' + k\bar{U}'\phi - \frac{gk^2\phi}{\bar{\Omega}}\right)\right] = 0 \tag{2.4b}$$

(Drazin and Reid, 1981) where the Δ operator is defined by

$$\Delta\left[f(z)\right] = \lim_{z\to z_*^+} f(z) - \lim_{z\to z_*^-} f(z)$$

and is applied at every z_* where the function $f(z)$ is discontinuous. In this case discontinuities can arise in any of $\bar{\rho}$, $\bar{U}$, or $\bar{U}'$. Strictly speaking, these limits should not be applied at constant elevations, z_*, but rather at interfaces around discontinuities in the background profiles that will be deformed by the presence of internal gravity waves; however since the wave amplitudes are small ($|Ak^2/\omega| \ll 1$), these *matching conditions* are in fact applied at constant elevations. For a fluid with continuous background horizontal flow, $\bar{U}$, the matching condition (2.4a) reduces to

$$\Delta\left[\phi\right] = 0 \tag{2.5}$$

and under the Boussinesq approximation the matching condition (2.4b) reduces to

$$\Delta\left[\rho_0\left(\bar{\Omega}\phi' + k\bar{U}'\phi\right) - \bar{\rho}\frac{gk^2}{\bar{\Omega}}\phi\right] = 0. \tag{2.6}$$

where ρ_0 is a characteristic density. If additionally the background density profile, $\bar{\rho}$, is continuous, (2.6) together with (2.5) further reduces to

$$\Delta\left[\bar{\Omega}\phi' + k\bar{U}'\phi\right] = 0. \tag{2.7}$$

Additional boundary conditions suitable for a vertically unbounded domain are also required. When examining the stability of a background shear flow this amounts to requiring bounded solutions such that internal waves, if they occur in the far field, propagate outward from the unstable region. The resulting equations form an eigenvalue problem in which the eigenvalue specifies the frequency and possibly the growth rate as a function of the horizontal wavenumber. The eigenfunction specifies the structure of the disturbance whose amplitude is arbitrary, though small.

When quantifying transmission in the tunnelling problem, the amplitude, frequency, and horizontal wavelength of an incident wave that propagates inward from the far field are specified and the boundary conditions require that, if waves transmit into the far field on the opposite side of the domain, then they must propagate outward. This is not an eigenvalue problem: both ω and k are independently specified. The resulting equations allow us to determine how the amplitude of the transmitted waves depends upon the amplitude of the incident waves.

2.3 Transmission Quantification

In the tunnelling problem the amplitude of a transmitted wave can be found in terms of an incident wave amplitude, frequency, and wavelength as well as any parameters associated with the problem, such as Richardson number.

When no shear is present and N is the same for transmitted waves as for incident waves we define a transmission coefficient,

$$T = \left| \frac{A_T}{A_I} \right|^2, \tag{2.8}$$

as the square magnitude of the ratio of transmitted to incident wave amplitude. This may be interpreted as the ratio of outgoing to incoming wave energy, $\langle E \rangle$, defined in the classical sense of the sum of the mean kinetic and available potential energy associated with the fluid parcels over one wavelength.

This was done by Sutherland and Yewchuk (2004), who in part studied the partial transmission and reflection of waves across a piecewise-constant N^2-barrier of depth L prescribed by

$$N^2(z) = \begin{cases} N_0^2 & |z| > \frac{L}{2} \\ 0 & |z| \leq \frac{L}{2} \end{cases} \tag{2.9}$$

which corresponds to a continuous background density profile of

$$\bar{\rho}(z) = \rho_0 \begin{cases} 1 - \frac{N_0^2}{g}\left(z - \frac{L}{2}\right) & z > \frac{L}{2} \\ 1 & |z| < \frac{L}{2} \\ 1 - \frac{N_0^2}{g}\left(z + \frac{L}{2}\right) & z < -\frac{L}{2} \end{cases} \tag{2.10}$$

as seen in Figure 1.1a. Defining $\Theta = \cos^{-1}(\omega/N_0)$ as the angle from the vertical at which wave propagate, they found the transmission coefficient to be

$$T = \left[1 + \left(\frac{\sinh(kL)}{\sin 2\Theta} \right)^2 \right]^{-1}. \tag{2.11}$$

They also studied the partial transmission and reflection of waves across a piecewise-constant mixed-N^2 profile where the background density is prescribed as

$$\bar{\rho}(z) = \rho_0 \begin{cases} 1 - \frac{{N_0}^2}{g} z & |z| > \frac{L}{2} \\ 1 & |z| \leq \frac{L}{2} \end{cases}. \tag{2.12}$$

Here the buoyancy frequency is the same as (2.9) except that $N^2 \rightarrow \infty$ at $z = \pm L/2$, seen in Figure 1.1b. The corresponding transmission coefficient was determined to be

$$T = \left[1 + \left(\frac{\sinh(kL)}{\sin 2\Theta}\right)^2 \left(1 + \frac{(kL)^2}{4\cos^2\Theta} - kL\coth(kL)\right)^2\right]^{-1}. \tag{2.13}$$

When shear is present in the background flow the transmission coefficient for the tunnelling problem cannot be defined as a ratio of wave energies. In shear flow, wave energy is not a conserved quantity but can be created or destroyed through interaction of the Reynolds stress with the background shear (see Section A.5). What is conserved for small-amplitude waves is the wave action, $\mathcal{A} = \frac{\langle E\rangle}{\Omega}$, defined by the ratio of the wave energy to the relative frequency (Eliassen and Palm, 1961; Andrews and McIntyre, 1976). More generally, the pseudoenergy is conserved which, in the small-amplitude limit, is the wave energy times the ratio of the absolute and relative frequencies, $\frac{\omega}{\Omega}$ (Andrews and McIntyre, 1978; Scinocca and Shepherd, 1992). Pseudoenergy is proportional to the wave action, but has the same units as energy. Since pseudoenergy is a conserved quantity, to classify the transmission of waves across a non-uniformly stratified shear flow, an appropriate definition of the transmission coefficient is the ratio of the transmitted to incident vertical flux of pseudoenergy. In the small-amplitude limit, the vertical flux of pseudoenergy is $c_{gz}\langle E\rangle\frac{\omega}{\Omega}$, the vertical group velocity times the pseudoenergy. After cancellation, using the relations found in Sections A.4 and A.5, the transmission coefficient is therefore defined as the ratio of transmitted to incident squared wave amplitude multiplied by the ratio of transmitted to incident vertical wavenumber,

$$T = \left|\frac{A_T}{A_I}\right|^2 \frac{m_T}{m_I}. \tag{2.14}$$

If there is no background shear and the buoyancy frequency is the same in both the incident and transmission regions, the vertical wavenumbers of transmitted and incident waves are identical and thus this definition of the transmission coefficient is equivalent to the ratio of transmitted to incident wave energy.

2.4 Stability of Background Profiles

Before performing the tunnelling calculation we first consider the stability of the prescribed background stratification and shear layer, with respect to a bulk Richardson number, defined as

$$\mathrm{Ri} = \left(\frac{N_0 L}{U_0}\right)^2. \tag{2.15}$$

Here N_0, U_0, and L are the characteristic buoyancy frequency, flow speed, and length scale, respectively, associated with the problem. A necessary (but not sufficient) condition for instability is that $\mathrm{Ri}_g < \frac{1}{4}$ (see for example, Drazin and Reid, 1981) in which the gradient Richardson number is defined as $\mathrm{Ri}_g = N^2(z)/\left[\bar{U}'(z)\right]^2$. The profiles considered here have $\mathrm{Ri}_g = 0$ in the shear region meaning that instability is possible. The purpose of this section is to determine how the stability of our prescribed stratification and background flow depend on the bulk Richardson number, Ri.

We consider a non-uniformly stratified shear layer of depth L in which N^2 is prescribed by (2.9) and the background flow by

$$\bar{U}(z) = \begin{cases} \frac{1}{2}U_0 & z > \frac{L}{2}, \\ \frac{U_0}{L} z & |z| < \frac{L}{2}, \\ -\frac{1}{2}U_0 & z < -\frac{L}{2}. \end{cases} \tag{2.16}$$

These profiles are illustrated in Figure 2.1a.

The solutions to the governing equation (2.2) for these profiles take the form

$$\phi(z) = \begin{cases} A_2 e^{im_- z} & z > \frac{L}{2} \\ B_1 e^{kz} + B_2 e^{-kz} & |z| < \frac{L}{2} \\ A_1 e^{im_+ z} & z < -\frac{L}{2}, \end{cases} \tag{2.17}$$

in which

$$m_{\pm} = \pm k \left[\frac{N_0^2}{\Omega_{\pm}^2} - 1\right]^{1/2}, \tag{2.18}$$

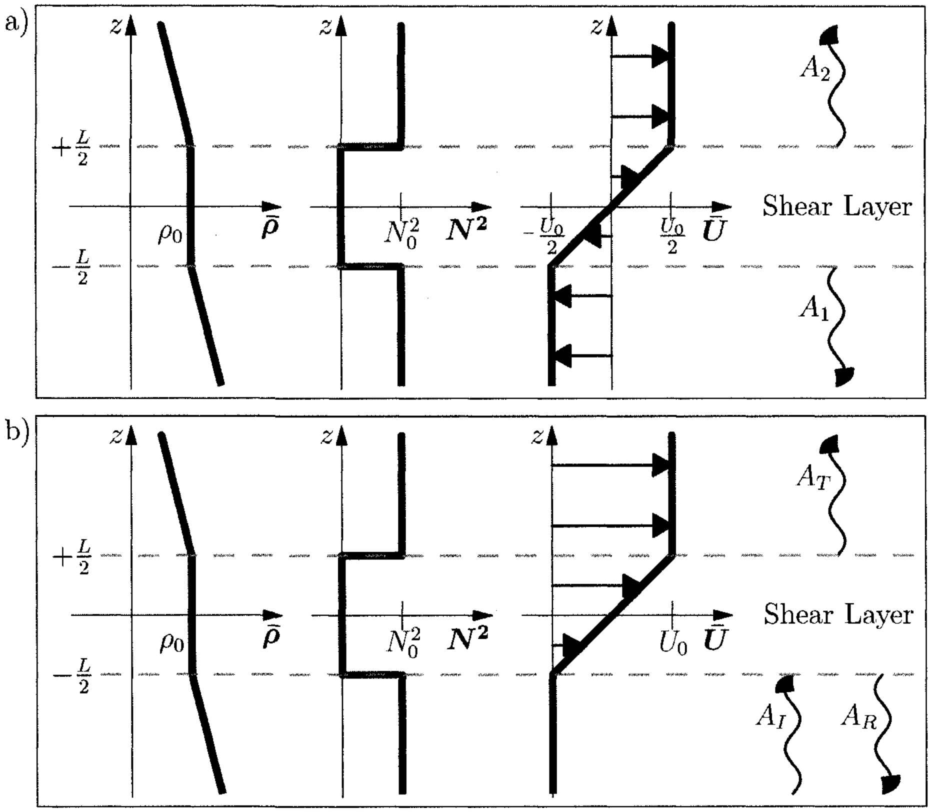

Figure 2.1: Background density (left), squared buoyancy frequency (middle), and velocity (right) profiles defined for the a) stability calculation and b) tunnelling calculation. In a) A_1, and A_2 are the amplitudes of the emitted disturbances. In b) A_I, A_R, A_T are the amplitudes of the incident, reflected, and transmitted waves respectively.

and

$$\Omega_{\pm} = \omega \pm kU_0/2. \tag{2.19}$$

If $|\Omega_{\pm}| \leq N_0$, the vertical wave number, $m_{\pm}$ is defined so that waves propagate away from the shear layer. For complex $m_{\pm}$, branch cuts are taken so that disturbances decay exponentially away from the shear layer. Applying matching conditions (2.5) and (2.7) at $z = \pm L/2$, gives an eigenvalue problem that predicts frequency as a function of wavenumber, k, through a cubic polynomial in ω^2:

$$\tilde{\omega}^6 + C_4\tilde{\omega}^4 + C_2\tilde{\omega}^2 + C_0 = 0. \tag{2.20}$$

Here the formula is given in non-dimensional form with $\tilde{\omega} = \omega L/U_0$. The coefficients $C_i(\tilde{k};\mathrm{Ri})$ for $i = 0, 2, 4$ are functions of the non-dimensional horizontal wavenumber $\tilde{k} = kL$ and the bulk Richardson number, Ri. These coefficients are

$$\begin{aligned}
C_4 &= \sinh^2(kL) - \left[\mathrm{Ri} + 2\left(\tfrac{kL}{2}\right)^2\right] - \left[\tfrac{\mathrm{Ri}\Gamma}{2\sinh(kL)}\right]^2, \\
C_2 &= \left(\tfrac{kL}{2}\right)^4 - \mathrm{Ri}\left(\tfrac{kL}{2}\right)^2 - \tfrac{1}{2}\mathrm{Ri}^2\Gamma^2 + \left(\tfrac{kL}{2}\right)^2 \tfrac{\mathrm{Ri}^2}{\sinh^2(kL)} \\
&\qquad + \left[\mathrm{Ri} + 2\left(\tfrac{kL}{2}\right)^2\right]\left[\tfrac{\mathrm{Ri}\Gamma}{2\sinh(kL)}\right]^2,
\end{aligned}$$

and

$$C_0 = -\left[\left(\tfrac{kL}{2}\right)^4 - \mathrm{Ri}\left(\tfrac{kL}{2}\right)^2 - \tfrac{1}{4}\mathrm{Ri}^2\Gamma^2\right]\left[\tfrac{\mathrm{Ri}\Gamma}{2\sinh(kL)}\right]^2$$

in which

$$\Gamma = \sinh(kL) + \tfrac{1}{\mathrm{Ri}}\left[\sinh(kL) - kL\cosh(kL)\right].$$

Of the three roots of (2.20) (in $\tilde{\omega}^2$), only one is physical and the others are spurious. The appropriate root is determined by taking the limit as $N_0 \to 0$ and selecting that which corresponds to the classic result for unstratified shear flow (Drazin and Reid, 1981):

$$\tilde{\omega}^2 = [(\tilde{k} - 1)^2 - e^{-2\tilde{k}}]/4. \tag{2.21}$$

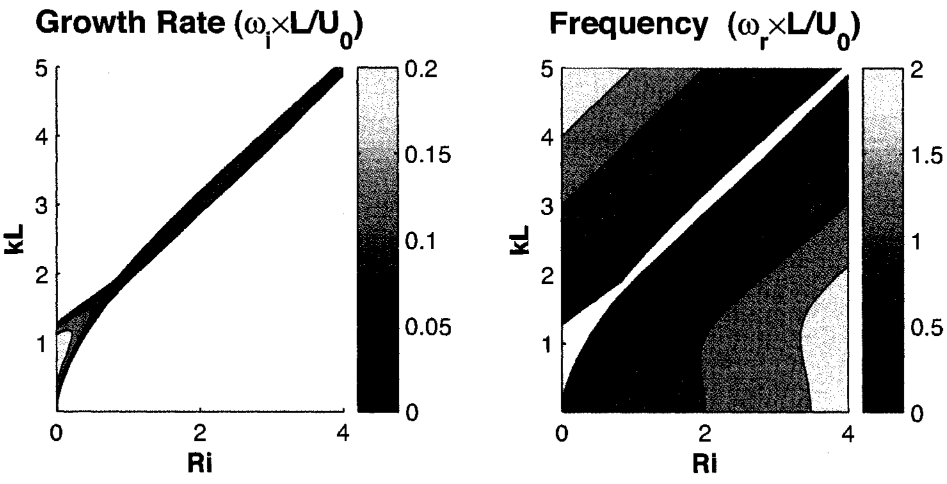

Figure 2.2: The non-dimensional growth rate ($\tilde{\omega}_i = \omega_i L/U_0$) and frequency ($\tilde{\omega}_r = \omega_r L/U_0$) defined by the physical root of (2.20).

The physical root, decomposed into its real and imaginary parts, is plotted in Figure 2.2. The left plot shows that the system is unstable for every value of Ri. However, the instability occurs over a decreasing range of kL about $\mathrm{Ri} = kL - 1$ as Ri increases. The marginal stability curves are given by

$$\mathrm{Ri} = (\tilde{k}/2)^2 - \left[(\tilde{k}/2)\coth(\tilde{k}/2) - 1\right]^2 \tag{2.22}$$

and

$$\mathrm{Ri} = (\tilde{k}/2)^2 - \left[(\tilde{k}/2)\tanh(\tilde{k}/2) - 1\right]^2 \tag{2.23}$$

when $\mathrm{Ri} \geq 1$.

From the right-hand plot we notice that when a wave is unstable the frequency of the wave, and thus the wave speed, is exactly zero; the speed matches the background flow speed at the midpoint of the shear. We also notice that the growth rate, $\tilde{\omega}_i$, of the instability decreases as Ri increases. So, although the gradient Richardson number, Ri_g, is zero in the shear region, instability is weak if the bulk Richardson number, Ri, is large enough.

We have not explicitly performed the stability calculation for the mixed-N^2 profile in which $\bar{\rho}$ is given by (2.12) rather than (2.10). The matching conditions make finding an analytic solution significantly more complex in this circumstance. However, we expect that the density jumps at $z = \pm L/2$ will serve further to stabilize the flow.

2.5 Transmission Predictions

In §2.4 we found that for large enough Ri, the instability growth rate of a piecewise-linear shear layer is smaller than the time for wave propagation across a coinciding uniform density region. We now consider internal wave tunnelling across a piecewise-linear shear layer in this large Ri limit. To this end we assume the prescribed background flow and density profiles are steady and study the circumstance of an internal gravity wave impinging from below upon an unstratified layer.

For conceptual convenience, we now shift to a frame of reference moving with the speed of the flow below $z = -L/2$. The shear flow profile is given by

$$\bar{U}(z) = \begin{cases} U_0 & z > \frac{L}{2} \\ \frac{U_0}{L}(z + \frac{L}{2}) & |z| < \frac{L}{2} \\ 0 & z < -\frac{L}{2} \end{cases} . \tag{2.24}$$

For this choice of velocity profile the relative frequency of an internal wave below $z = -L/2$ is the same as its absolute frequency, ω. Above $z = +L/2$ the relative frequency is given by

$$\Omega = \omega - kU_0. \tag{2.25}$$

2.5.1 Transmission across an N^2-barrier

We begin by examining internal wave tunnelling across an N^2-barrier with N^2 given by (2.9) and shear flow given by (2.24) as plotted in Figure 2.1b. We suppose that a wave with given k, ω, and streamfunction amplitude, A_I, is incident upon the shear region from below. The phase speed of this wave is $c = \omega/k$. Without loss of generality, we only allow positive values for ω so that the horizontal direction of wave propagation is entirely determined by the sign of k.

Similar to (2.17), solutions to the Taylor-Goldstein equation (2.2) in each piecewise-linear region take the form

$$\phi(z) = \begin{cases} A_T e^{-im_T z} & z > \frac{L}{2} \\ B_1 e^{kz} + B_2 e^{-kz} & |z| < \frac{L}{2} \\ A_I e^{-im_I z} + A_R e^{im_I z} & z < -\frac{L}{2} \end{cases} \tag{2.26}$$

in which

$$m_I = |k \tan \Theta| \text{ and } m_T = |k \tan \Phi| \tag{2.27}$$

are vertical wavenumbers for the incident and transmitted waves, respectively. We have defined

$$\Theta = \cos^{-1}\left(\frac{\omega}{N_0}\right) \text{ and } \Phi = \cos^{-1}\left(\frac{\Omega}{N_0}\right). \tag{2.28}$$

These represent the angle between lines of constant phase and the vertical for incident and transmitted waves respectively. Notice that ϕ in (2.26) includes solutions for both incident and reflected waves below $z = -L/2$. Applying the matching conditions (2.5) and (2.7) at $z = \pm L/2$ gives a system of four equations and five unknowns.

Solving these for the transmitted amplitude, A_T, in terms of the incident amplitude, A_I, gives a transmission coefficient, T, defined as the ratio of transmitted to incident pseudoenergy flux given by

$$T = \left|\frac{A_T}{A_I}\right|^2 \left|\frac{\tan \Phi}{\tan \Theta}\right|, \tag{2.29}$$

in which we have used (2.14) with the relationship between vertical wavenumber and propagation angle, (2.27). Likewise we may define the reflection coefficient, R, to be the magnitude of the reflected to incident pseudoenergy flux. In this case the ratio of vertical wavenumbers cancels and we find $R = |A_R|^2/|A_I|^2$. Tests show that the relationship $T + R = 1$ holds, as expected.

After extensive algebraic manipulation the transmission coefficient is found to be

$$T^{-1} = 1 + \frac{\left\{\sinh(kL) + \frac{1}{\mathrm{Ri}}\left[\sinh(kL) - kL\cosh(kL)\right]\right\}^2 + \alpha^2 - \frac{1}{\mathrm{Ri}}\beta^2}{|\sin 2\Theta \sin 2\Phi|}, \tag{2.30}$$

in which

$$\alpha = \sin(\Theta \mp \Phi) \tag{2.31}$$

and

$$\beta = (\cos\Theta + \cos\Phi)\sinh(kL). \tag{2.32}$$

The angles in (2.31) are subtracted if $\tan\Theta$ and $\tan\Phi$ are of the same sign and they are summed otherwise. Together with (2.25) and (2.28), (2.30) reduces to (2.11) in the limit as $\mathrm{Ri} \to \infty$ (corresponding to $U_0 \to 0$ and $\Phi \to \Theta$ at fixed L) and so these results are consistent with those of Sutherland and Yewchuk (2004). For any finite Ri (in which U_0/L is fixed) we find $T \to 1$ for fixed k as $L \to 0$. In this instance the background is reduced to constant N^2 with vanishingly small shear. Note that for finite Ri the numerator can be negative, corresponding to $T > 1$. This corresponds to waves acting in near resonance with unstable modes so that transmitted waves can draw energy from both the incident waves and the mean flow. This occurs only for $\mathrm{Ri} \ll 1$ in which case the mean flow is strongly unstable.

Contour plots of T as a function of kL and ω/N_0 in four cases, each with different values of Ri, are given in Figure 2.3a. In the upper-left plot $\mathrm{Ri} = 10^6$ is chosen to be so large that the shear flow is effectively non-existent: $U_0 \simeq 0$. As expected in this limit, T approaches that found for a N^2-barrier by Sutherland and Yewchuk (2004).

For smaller Ri, Doppler-shifting by the shear flow plays an increasingly significant role. As required by (2.26), there is no transmission of waves if the magnitude of the relative frequency of waves above $z = +L/2$ exceeds N_0. For non-trivial solutions, this forces the absolute frequency and wavelength of

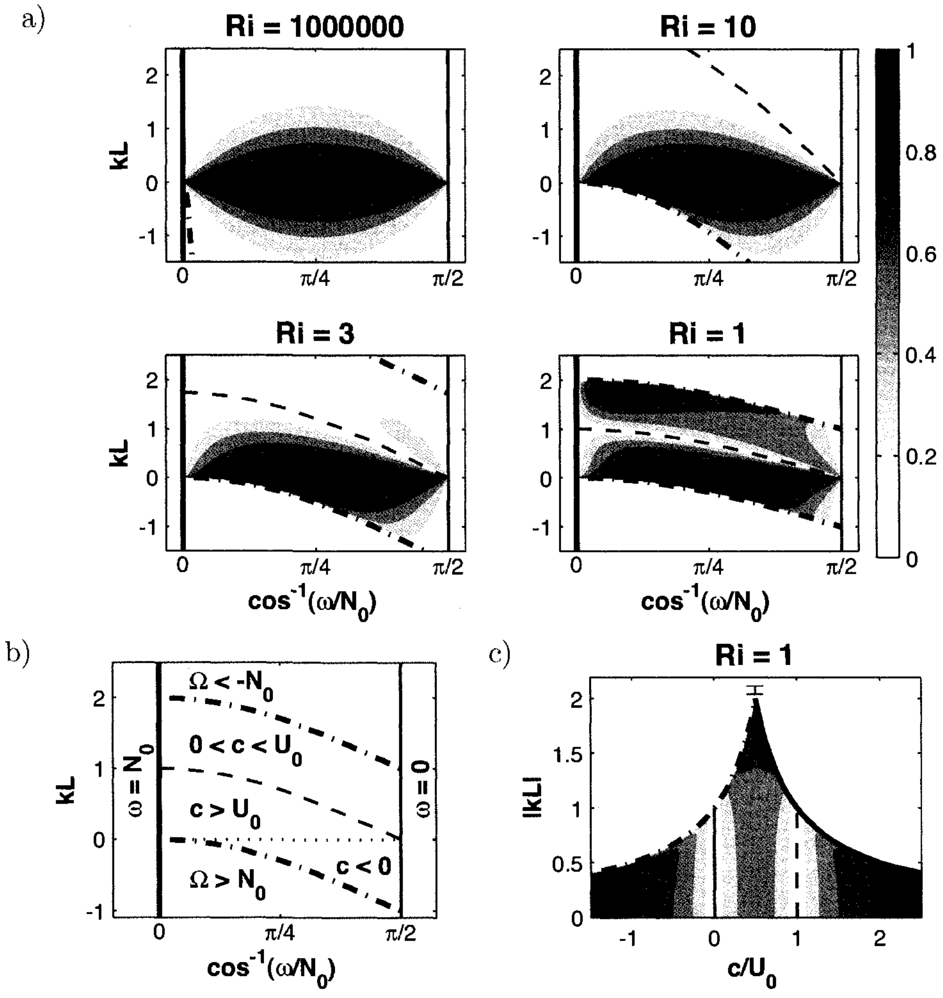

Figure 2.3: a) Contour plots of the transmission coefficient, T, for internal gravity waves traversing an N^2-barrier as a function of frequency and wavenumber for several values of the bulk Richardson number, Ri, as indicated. b) Schematic formulae defining the bounding lines in the contour plots. Wave transmission is bounded between the solid and dash-dotted lines where the relative frequency of incident and transmitted waves respectively equal the buoyancy frequency. The dashed line separates waves that encounter a critical level and those that do not. c) Values of the transmission coefficient as a function of wavenumber and phase speed for Ri = 1.

the incident waves to lie within a parameter regime shown schematically in Figure 2.3b. The allowable frequencies and wavelengths are bounded by the solid lines $\omega = 0$, $\omega = N_0$ and the dash-dotted lines $\Omega = \pm N_0$. This bounded region can be further separated into two sub-regimes separated by a dashed line which denotes waves whose relative frequency is $\Omega = 0$. Below this line incident waves propagate faster than U_0 or in the opposite direction from the flow above $z = +L/2$ (*i.e.* $c < 0$) and therefore they do not encounter a critical level. For parameters above the dashed line, waves propagate with phase speed $0 < c < U_0$ and thus encounter a critical level within the shear layer.

From Figure 2.3a we find that, for all Ri, near perfect transmission occurs for waves with $|kL| \ll 1$. For the smaller values of Ri, the transmission coefficient is exactly zero along the dashed line where the horizontal phase speed of the incident waves matches the flow speed above the shear layer, U_0. Such behaviour may be anticipated from the heuristic prediction that waves cannot penetrate above a critical level. Surprisingly, however, for Ri $= 1$ and 3 we see transmission for internal waves which encounter a critical level within the shear layer. Incident waves are able to cross the critical level because $N^2 = 0$ in the shear region, and so all disturbances are evanescent, not wave-like there. We find nearly perfect transmission for waves with $kL \lesssim 2$ and $\omega \lesssim N_0$ if Ri $= 1$. To examine the transmission spike, we plot the transmission contours for Ri $= 1$ as a function of the incident phase speed and wavenumber in Figure 2.3c. We find the transmission spike occurs for waves with phase speed equal to the midpoint of the shear ($c = U_0/2$). Waves within the transmission spike have wavenumbers and frequencies that are nearly resonant with those of unstable modes. Indeed, Figure 2.2 shows that unstable modes occur when $kL \simeq 2.08$ when Ri $= 1$. The full range of unstable modes is indicated in Figure 2.3c by the error-bar and lies outside, but close to, the allowable parameter range for internal waves. Although we see a large transmission spike for propagating internal waves, disturbances which lie in the range of unstable modes are evanescent at all levels in the flow for Ri = 1.

For still smaller Ri, the parameter range for unstable modes increases to lie within the allowable range for propagating internal waves. In this case, we expect to see transmission coefficients exceeding unity, meaning that the incident waves draw energy from the mean flow and so transmit across the shear at larger amplitude. In the absence of incident waves, this is the process of *over-reflection* (*i.e.* Lindzen and Tung, 1976). We have not examined this circumstance in detail because the time-scale for instability compared with the time for waves to cross the shear layer is so small that it is hard to imagine a realistic circumstance in which incident waves might encounter the unstable shear layer before it develops nonlinearly.

2.5.2 Transmission across a locally mixed region

In the circumstance considered above, $\bar{\rho}$ varies continuously, even though its slope is discontinuous at $z = \pm L/2$. More realistically, localized mixed regions within a stratified fluid are better represented by the discontinuous density profile given by (2.12), seen in Figure 1.1b. Thus we now examine internal wave tunnelling across such a mixed-N^2 profile.

We proceed exactly as in the preceding section to find solutions to (2.2) given by (2.26). The difference is that we now must apply the matching conditions (2.5) and (2.6) for discontinuous density profiles to determine the transmitted amplitude in terms of the incident wave amplitude. The transmission coefficient is defined as in (2.29) and is determined to be

$$T^{-1} = \frac{\left|[ab - \cos\Theta\cos\Phi]\sinh(kL) - [a\cos\Theta - b\cos\Phi]\cosh(kL)\right|^2}{|\sin 2\Theta \sin 2\Phi|}, \quad (2.33)$$

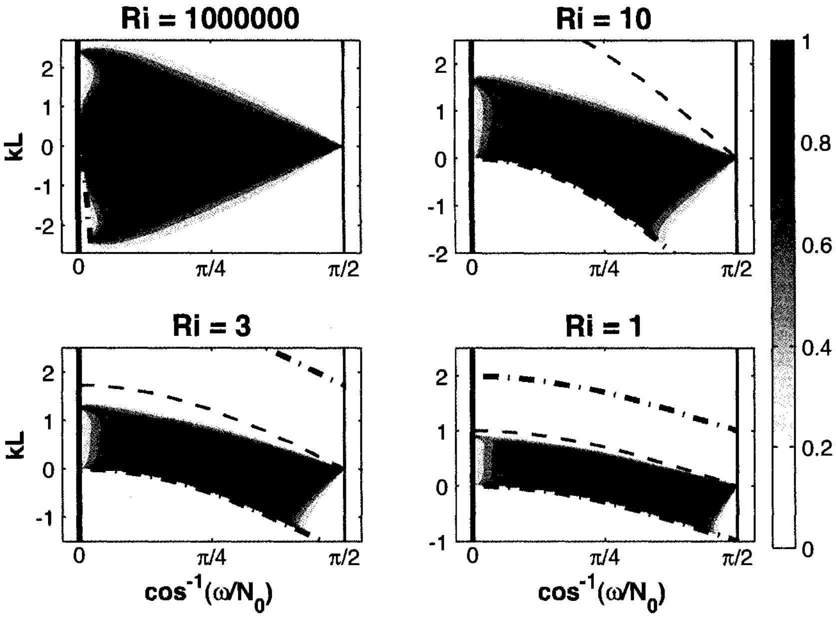

Figure 2.4: As in 2.3a, but for internal gravity waves traversing a mixed-N^2 profile.

in which

$$a = \frac{1}{\sqrt{\mathrm{Ri}}} - \frac{kL}{2}\sec\Phi + i\sin|\Phi| \tag{2.34}$$

and

$$b = \frac{1}{\sqrt{\mathrm{Ri}}} - \frac{kL}{2}\sec\Theta - i\sin|\Theta| \tag{2.35}$$

We do not explicitly manipulate this equation to be of the same form as (2.30) because of its complexity, but we do plot contours of the transmission coefficient in Figure 2.4.

In these plots the lines that create a bounding box and the dashed lines are defined exactly as in the previous section. In the case of negligibly small shear ($\mathrm{Ri} = 10^6$) transmission is the same as that found for a locally mixed region by Sutherland and Yewchuk (2004). One obvious difference between the N^2-barrier and mixed-N^2 case is the appearance of a transmission spike for waves with $\omega \lesssim N_0$ and $kL \simeq 2.4$. This occurs due to resonant coupling of the propagating internal gravity waves and interfacial waves which are situated at the density jumps above and below the shear layer.

For smaller Ri, this transmission spike remains as the dominant feature causing transmission to be much greater than in the N^2-barrier case. In fact, transmission is nearly perfect for almost half the allowable range of frequency and wavenumber.

For small Ri, the most notable difference between transmission in the N^2-barrier and mixed-N^2 case is the lack of transmission above the dashed line where incident waves encounter a critical level. The presence of density jumps bounding a shear layer apparently inhibits transmission across critical levels in uniform-density fluid.

Chapter 3

Large Amplitude Tunnelling

3.1 Introduction

In the previous chapter only internal waves with vanishingly small amplitude were considered. This was necessary so that linear theory could be applied. In this chapter the effect that finite amplitude has on the transmission of internal waves across an N^2-barrier is explored. The propagation and transmission of internal waves is examined using a fully nonlinear numerical model that simulates the two dimensional Boussinesq equations of motion.

In Section 3.2 the numerical method is described. Two techniques for quantifying the time dependent transmission of internal waves are developed in Section 3.3. The stability requirements for simulations of an initially compact internal wavepacket are explained in Section 3.4. Finally, in Section 3.5 the effect of amplitude on internal wave tunnelling is described.

3.2 Numerical Method

The numerical method used solves the discretized form of the following coupled, fully nonlinear equations of the total vorticity, ζ_T, and perturbation density, ρ, fields

$$\frac{\mathrm{D}\zeta_T}{\mathrm{D}t} = \frac{g}{\rho_0}\frac{\partial \rho}{\partial x} + \nu \nabla^2 \zeta \tag{3.1a}$$

$$\frac{\mathrm{D}\rho}{\mathrm{D}t} = -w\frac{\mathrm{d}\bar{\rho}}{\mathrm{d}z} + \kappa \nabla^2 \rho. \tag{3.1b}$$

Here, ν is the kinematic viscosity and κ is a molecular diffusivity. These equations of motion are the same as the governing equations for internal waves (A.13) developed in Section A.1 except that they contain diffusion terms which are required for numerical stability. Numerical simulations step in time using a second-order leapfrog method with an Euler backstep taken at regular intervals to avoid a computational mode. Spatial derivatives are computed using a centred finite differencing technique. More details of the method can be found in Sutherland and Peltier (1994).

Simulations are initialized with no background horizontal mean flow (*i.e.* $\bar{U}(z) \equiv 0$) and a N^2-barrier background buoyancy profile given by (2.9). A horizontally and vertically compact wavepacket centred a distance of $|z_0|$ below the middle of the tunnelling region is superimposed on the background fields. The horizontal and vertical wavenumbers, k and m, of waves within the packet are set so that the wavepacket moves to the right and upward toward the tunnelling region in time. Gaussian wavepackets with horizontal and vertical standard deviations of σ_x and σ_z respectively are considered in this study. The perturbation density, ρ, and vorticity, ζ, fields of the wavepacket are prescribed initially using the linear polarization relations found in table A.1 for a streamfunction given by

$$\psi\left(x, z, 0\right) = A_\psi e^{-\frac{1}{2}\left[\left(\frac{x}{\sigma_x}\right)^2 + \left(\frac{z-z_0}{\sigma_z}\right)^2\right]} \cos\left(kx + mz\right). \tag{3.2}$$

Although this initialization is not an exact solution to the inviscid form of (3.1), if $|\sigma_x k| \gg 1$ and $|\sigma_z m| \gg 1$ the envelope of the wavepacket is sufficiently large that theory can be applied as if waves were monochromatic. In addition to the wavepacket, a horizontal flow associated with waves must also be prescribed (Sutherland, 2001). For horizontally periodic waves this would be the wave-induced mean-flow, $\mathcal{M} = -\langle \xi\zeta \rangle$ (see A.45). The horizontally compact wavepackets studied here, however, do not induce a mean flow over the entire extent of the domain although a localized horizontal flow over the extent of a wavepacket is induced. This localized flow is prescribed by computing the correlated field $-\xi\zeta$ everywhere in the domain and superimposing it on the horizontal velocity field. Control simulations confirm the use of this initialization: as waves propagate, the horizontally averaged flow moves upward with the waves leaving behind no residual stationary mean flow.

In practice, the length and time scales of simulations are set so that $k = 1.0$ and $N_0 = 1.0$, however, results are presented in terms of units of inverse horizontal wavenumber, k^{-1}, and inverse buoyancy frequency, N_0^{-1}, or horizontal wavelength, $\lambda_x = 2\pi/k$, and buoyancy period, $T_B = 2\pi/N_0$, where convenient. The diffusion parameters of (3.1) are chosen so the effect of diffusion on the dynamics is negligible but the code remains numerically stable. These terms are necessary to eliminate the growth of small scale numerical noise. In these simulations, a Reynolds number of 10000 and a Prandl number of 1.0 are used (*i.e.* $\nu = \kappa = 10^{-4}\, N_0 k^{-2}$). These numbers are not representative of realistic kinematic viscosities and molecular diffusivities for geophysical flows. However, the process of diffusion is irrelevant to the dynamics being studied. The values chosen are sufficient to allow the initial wavepacket to essentially evolve as if it were in an inviscid fluid whereas realistic values would require finer grid resolutions, and thus longer running times, without providing additional insight.

In nearly all simulations the wavepacket is initially centred at $z_0 = -3\,\sigma_z$ where the vertical extent of the wavepacket is set with a standard deviation of $\sigma_z = 10\,k^{-1}$. The domain is a horizontally periodic channel with free-slip conditions on the upper and lower boundaries. The extent of the domain is set to be much larger than the extent of the wavepacket itself so that interactions with the boundaries are negligible. A domain height of $204.8\,k^{-1}$ is used so that the amplitude of waves at both boundaries remains small over the entire duration of simulations. Unless otherwise specified, the horizontal extent of the domain is typically $16\,\lambda_x$ (or $\sim 100.5\,k^{-1}$) for wavepackets initialized with $\sigma_x = 10\,k^{-1}$. The basic state fields are represented at evenly spaced vertical levels of $0.05\,k^{-1}$ by spectral coefficients of the horizontal structure. This vertical resolution can accurately represent vertical wavenumbers of up to approximately $15.5\,k$. The horizontal resolution is set to resolve waves with horizontal wavenumber up to $8\,k$. Simulations proceed by advancing $0.01\,N_0^{-1}$ in time with an Euler backstep taken at regular intervals of $0.2\,N_0^{-1}$. Simulations with increased resolutions and domain sizes were run and show little to no change in the resulting transmission coefficients.

3.3 Transmission Quantification

Because simulations that advance in time are required to study the effect of amplitude on transmission, the magnitude of the transmission coefficient cannot be measured as it was in Chapter 2 where quantities, such as energy, could be determined that were independent of time. In this portion of the study two different measures of transmission were used. The first method is the simplest conceptually as it is a ratio of spatially integrated pseudoenergies, or, equivalently, energies in cases with no mean background flow. Under this method transmission is defined as

$$T_{\mathcal{E}}\left(t\right) = \frac{\mathcal{E}_{\text{Trans}}}{\mathcal{E}_{\text{Total}}} \tag{3.3}$$

where

$$\mathcal{E}_{\text{Trans}}\left(t\right) = \int_{\frac{L}{2}}^{\infty}\int_{-\infty}^{\infty} \mathcal{E}\left(x, z, t\right)\,\mathrm{d}x\,\mathrm{d}z \tag{3.4a}$$

and

$$\mathcal{E}_{\text{Total}}(t) = \int_{-\infty}^{\infty}\int_{-\infty}^{\infty} \mathcal{E}(x, z, t)\,\mathrm{d}x\,\mathrm{d}z \tag{3.4b}$$

are the spatially integrated pseudoenergy field in the transmission region (everywhere above the tunnelling region) and the total domain respectively.

The second method used to quantify transmission is similar to (2.14) of the previous chapter as it is a ratio of time integrated pseudoenergy fluxes. Under this method transmission is defined as

$$T_{\mathcal{F}}(t) = \frac{\mathcal{F}_{\text{Trans}}}{\mathcal{F}_{\text{Total}}} \tag{3.5}$$

where

$$\mathcal{F}(t) = \int_{0}^{t}\int_{-\infty}^{\infty} \mathcal{F}_z\left(x, \tfrac{L}{2}, \tau\right)\,\mathrm{d}x\,\mathrm{d}\tau \tag{3.6}$$

is the time integrated vertical flux of pseudoenergy through the vertical level $z = L/2$. The difficulty with this method is determining $\mathcal{F}_{\text{Total}}$ because the entire wavepacket does not pass through a single vertical level before the leading edge has begun to reflect off the N^2-barrier and propagate in the opposite direction. To find this quantity a second control simulation is run with identical parameters to the first except that the background buoyancy frequency is constant ($N(z) = N_0$). Using either method the transmission is initially variable as the wavepacket interacts with the tunnelling region but eventually reaches a constant value once the bulk of the wavepacket has either reflected or transmitted. In all cases both methods give consistent results, to within 1% of each other.

3.4 Stability Criteria

In order to quantify accurately the transmission of internal waves, wavepackets must remain stable. This means internal waves cannot overturn and break and an initially compact wavepacket must remain coherent throughout the duration of a numerical simulation.

Internal waves are statically unstable if

$$\frac{\partial}{\partial z}\left[\bar{\rho}\left(z\right)+\rho\left(x,z,t\right)\right]>0. \tag{3.7}$$

That is, the sum of the vertical gradient of the background density and perturbation density fields is positive. When this occurs, heavy fluid lies on top of lighter fluid allowing waves to overturn and break. Defining a perturbation change in buoyancy frequency as

$$\Delta N^{2}\left(x,z,t\right)=-\frac{g}{\rho_{0}}\frac{\partial\rho}{\partial z} \tag{3.8}$$

a wavepacket is said to have broken the *overturning condition* if

$$\Delta N^{2}\left(x,z,t\right)<-N_{0}^{2} \tag{3.9}$$

at any point in the domain.

Sutherland (2001) showed that an initially compact wavepacket can subdivide into multiple diverging wavepackets if another condition, known as the *self-acceleration condition*, is broken. This second condition, which is the first to be broken for non-hydrostatic waves, requires that the magnitude of the horizontally averaged localized wave-induced mean-flow, which for horizontally compact waves is defined as

$$\mathcal{M}_{\sigma}\left(z,t\right)=-\left\langle\xi\zeta\right\rangle_{\sigma_{x}}=\frac{1}{2\sigma_{x}}\int_{-\infty}^{\infty}\left(-\xi\zeta\right)\,\mathrm{d}x, \tag{3.10}$$

remain less than the horizontal group velocity of the wavepacket over the duration of the simulation. Explicitly, the self-acceleration condition is said to be broken if

$$\mathcal{M}_{\sigma}>c_{g_{x}} \tag{3.11}$$

at any height in the domain where c_{g_x} is the horizontal group velocity. In order to measure transmission accurately, only numerical simulations where neither condition (3.9) nor (3.11) is broken can be used to study the effect of amplitude on internal wave transmission. These conditions apply to propagating waves and can only be applied outside of the tunnelling region where $N^2 = 0$ and waves are evanescent. The use of these stability conditions effectively creates an upper limit on the amplitude range that can be studied.

Applying the definition for the wave-induced mean-flow in (3.10) to an initial Gaussian wavepacket prescribed by (3.2) and using the properties of internal waves found in Table A.1, the initial wave-induced mean-flow of the simulations is

$$\mathcal{M}_\sigma(z) \approx U_0 e^{-\left(\frac{z-z_0}{\sigma_z}\right)^2} \quad \text{with} \quad U_0 = \frac{\sqrt{\pi}}{4}\frac{N_0}{k}(A_\xi k)^2 \sec\Theta. \tag{3.12}$$

Normalizing with the horizontal group velocity from (A.32a) the maximum initial wave-induced mean-flow is

$$\frac{U_0}{c_{g_x}} = \frac{4\pi^2\sqrt{\pi}}{\sin^2 2\Theta}\left(\frac{A_\xi}{\lambda_x}\right)^2. \tag{3.13}$$

Substituting (3.13) into (3.11), the initial wavepacket amplitude must satisfy

$$\frac{A_\xi}{\lambda_x} \lesssim 0.12|\sin 2\Theta| \tag{3.14}$$

to meet the self-acceleration condition. Unfortunately, this restriction on the initial wave amplitude is not sufficient to guarantee the self-acceleration condition will not be broken over the duration of a numerical simulation.

Figure 3.1 shows the time evolution of the normalized wave-induced mean-flow, $\mathcal{M}_\sigma/U_0$, for several simulations of compact wavepackets in uniform background stratification. In each case, the results are translated into a frame of reference moving with the vertical group velocity, c_{g_z}. These horizontally compact simulations are similar to the horizontally periodic simulations (*i.e.* $\sigma_x k \to \infty$) studied by Sutherland (2006). Figure 3.1a shows the results of three simulations with vertical wavenumbers of $m = -0.4, -0.7$, and $-1.4\,k$ and an initial amplitude of $A_\xi = 0.01\,\lambda_x$. In all three simulations the wave-induced

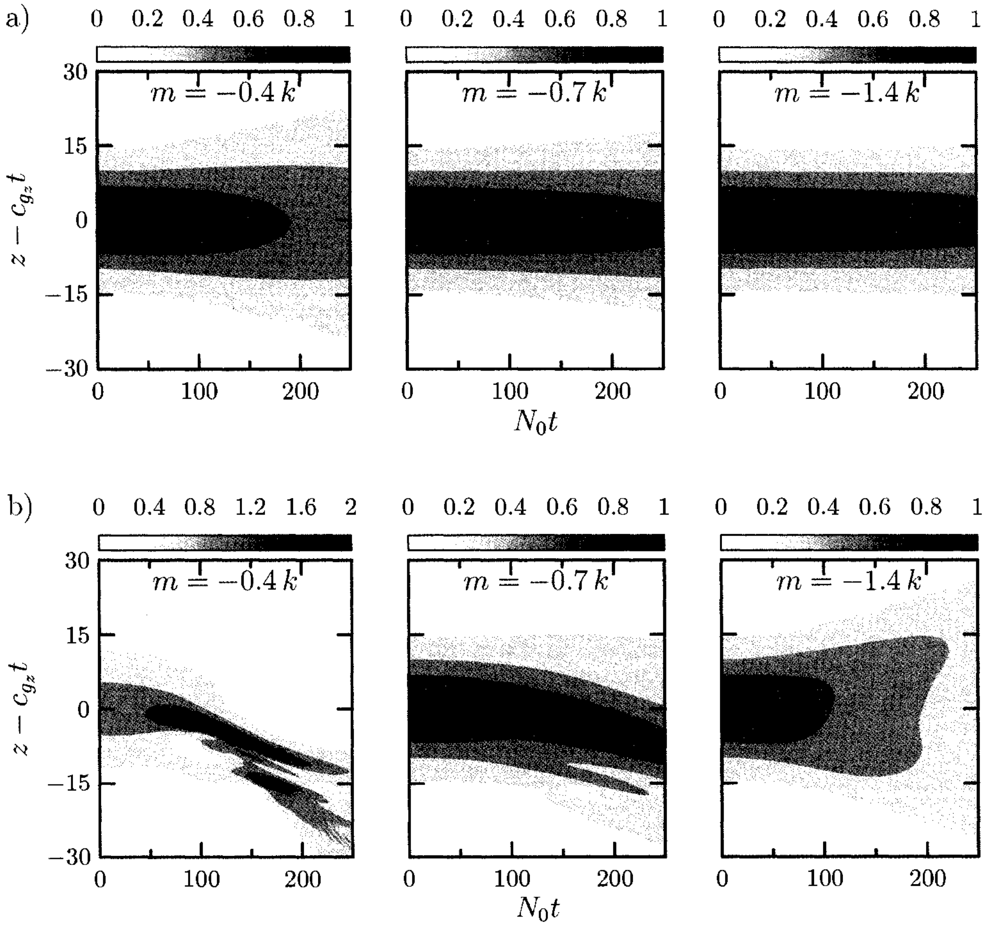

Figure 3.1: The time evolution of the wave-induced mean-flow, $\mathcal{M}_\sigma/U_0$ given by (3.10), for fully nonlinear numerical simulations of a horizontally compact wavepacket in uniform background stratification. The vertical coordinate is shifted to move with c_{g_z}. Wavepackets used in a) are initialized with $A_\xi = 0.01\,\lambda_x$, $\sigma_x = \sigma_z = 10\,k^{-1}$, and $m = -0.4, -0.7,$ and $-1.4\,k$ in the left, centre, and right panels respectively. The wavepackets used in b) are the same as in a) except that $A_\xi = 0.10\,\lambda_x$.

mean-flow is peaked along the level $z = c_{g_z}t$, confirming that small amplitude wavepackets propagate vertically at the vertical group velocity. The vertical structure of the wave-induced mean-flow in these simulations broadens and decreases in peak amplitude due to linear dispersion with the left panel, where $|\sigma_z m| = 4$ is the smallest, exhibiting the most dispersion. Larger amplitude simulations with $A_\xi = 0.08\,\lambda_x$ in Figure 3.1b show qualitatively different behaviour. In the left panel where $m = -0.4\,k$ the wavepacket decelerates and narrows beginning at $t \approx 100\,N_0^{-1}$ so that the maximum value of $\mathcal{M}_\sigma$ nearly triples the initial value ($\sim 2.95\,U_0 = 2.78\,c_{g_x}$) and breaks the self-acceleration condition. In the right panel where $m = -1.4\,k$ the wavepacket continues to propagate at the vertical group speed although the wave-induced mean-flow broadens more quickly and the maximum value drops by more than half due to nonlinear dispersive effects. The centre panel shows aspects of both behaviours at the critical value of $m = -0.7\,k$ (*i.e.* $\Theta = 35°$) where the vertical group velocity is largest. These results are consistent with those of Sutherland (2006) except that they observed the change in wavepacket behaviour at large amplitudes beginning earlier at $t \approx 50\,N_0^{-1}$. It seems that restricting the horizontal extent of wavepackets reduces the effect of self-acceleration caused by interactions between waves and the wave-induced mean-flow.

Since the maximum value of $\mathcal{M}_\sigma$ increases during the evolution of some wavepackets, (3.14) is not sufficient to insure that the self-acceleration condition is not broken during the course of a simulation. Additionally, in cases with a N^2-barrier stratification the maximum amplitude of the wave-induced mean-flow can increase even further. As waves reflect off the barrier, the superposition of the incident and reflected wavepackets causes the maximum wave amplitude to increase. Linear theory predicts the maximum value of $\mathcal{M}_\sigma$ will increase by a factor of $\left(1 + \sqrt{R}\right)^2$ (*i.e.* for a perfectly reflected wavepacket, the wave amplitude doubles and so the amplitude of the wave-induced mean-flow quadruples). In practice, simulations where the self-acceleration condition is broken and waves do not overturn have lower transmission values than simulations with slightly smaller amplitude wavepackets that remain stable. This is due to a significant portion of the initial wavepacket changing speed and direction early on and thus not reaching the N^2-barrier during a simulation.

3.5 Numerical simulation results

To examine the effect of amplitude on the transmission of internal waves through an N^2-barrier, multiple simulations with initial wave amplitude ranging between $A_\xi = 10^{-4}\,\lambda_x$ and $A_\xi = 0.1\,\lambda_x$ were run. For the majority of simulations a barrier width of $L = 1.0\,k^{-1}$ was used.

Figure 3.2 shows the evolution of both small and finite amplitude horizontally compact wavepackets interacting with a N^2-barrier centred around $z = 0\,k^{-1}$ depicted by the gray line. Snapshots of the vertical displacement field taken from simulations at time $t = 0, 85,$ and $170\,N_0^{-1}$ (or $t \approx 0, 13.5,$ and $27\,T_B$) for wavepackets initialized with $A_\xi = 0.01\,\lambda_x$ (small-amplitude) and $A_\xi = 0.08\,\lambda_x$ (finite-amplitude) are shown in Figure 3.2a and Figure 3.2b respectively. Both wavepackets are also initialized with a vertical wavenumber of $m = -1.0\,k$ or equivalently a propagation angle of $\Theta = -45°$. Snapshots of wavepackets at other vertical wavenumbers can be found in Appendix B. The two leftmost panels show the initial normalized vertical displacement field for both simulations. These appear identical because the contour levels in the large-amplitude case are 8 times larger. For ease of visualization, the snapshots are taken in a frame of reference moving with the linearly predicted horizontal group velocity so that wavepackets are centred in each panel. In both simulations the initial wavepacket splits into two parts; an upward propagating transmitted portion and a downward propagating reflected portion.

Focusing on the small-amplitude simulation, the centre panel shows the

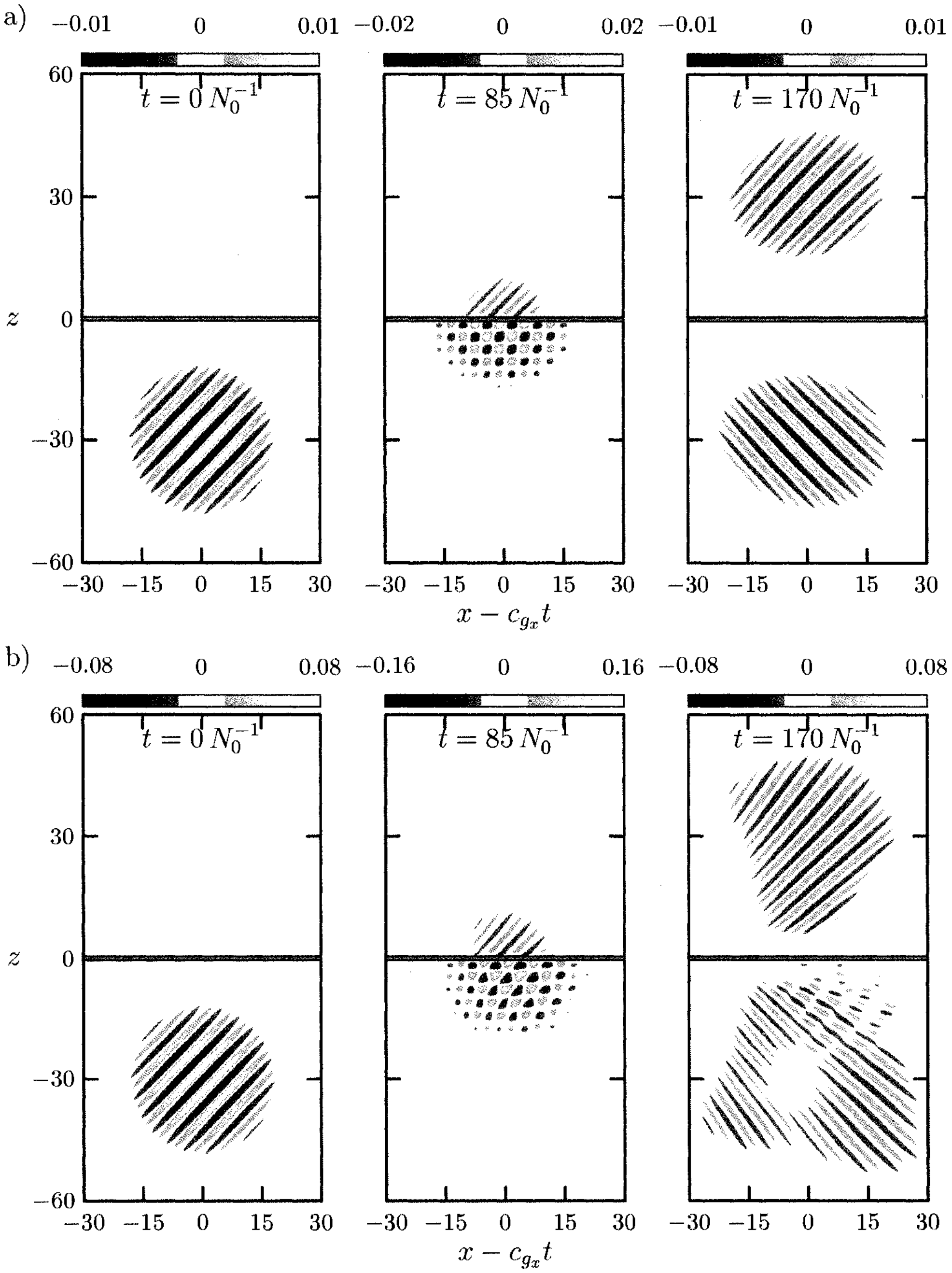

Figure 3.2: Results of fully nonlinear numerical simulations of a wavepacket given initially by (3.2) impinging on a N^2-barrier of width $L = 1.0\,k^{-1}$ depicted by the gray centre line. Wavepackets are initialized with $m = -1.0\,k$, $\sigma_x = \sigma_z = 10\,k^{-1}$, and $A_\xi = 0.01\,\lambda_x$ in a), and $A_\xi = 0.08\,\lambda_x$ in b). Contours are of the normalized vertical displacement field, ξ/λ_x, at $t = 0, 85,$ and $170\,N_0^{-1}$ in the left, centre, and right panels respectively. The domain is shifted by the horizontal group velocity, c_{g_x}, so that wavepackets remain centred.

wavepacket midway through reflecting off and tunnelling through the N^2-barrier. The superposition of the incident and reflected wavepackets results in a crosshatch pattern with the maximum amplitude of vertical displacements nearly doubled. The superposition is such that heights with no vertical displacement occur at intervals of $\frac{1}{2}\lambda_z$ and columns with no vertical displacement are separated by $\frac{1}{2}\lambda_x$. The right panel shows the wavepacket after separating into the two portions. Both portions have propagated vertically at a speed nearly equal to the vertical group speed which in this case is $|c_{g_z}| \approx 0.35\, N_0 k^{-1}$ so that the transmitted portion is centred at $z \approx 30\, k^{-1}$ and the reflected portion returns to the initial height after $t = 170\, N_0^{-1}$. The most obvious change from the initial state is the increased horizontal spread of the wavepackets. This increase is caused by the linear dispersion of the internal waves as they propagate. Unlike the horizontal extent, the vertical extent of the wavepacket has increased very little, meaning that linear dispersion has a greater effect in the horizontal direction than in the vertical direction for waves with $|\Theta| = 45°$. This effect is opposite for wavepackets with propagation angles smaller than $|\Theta| = 35°$ which have the highest vertical group speed (see Figure B.1).

Using (3.5) to calculate the fraction of the energy transmitted through the N^2-barrier, the transmission coefficient in the small-amplitude case is found to be $T = 42.3\%$, which is approximately 0.7% greater than the linearly predicted value for horizontal plane waves (2.11). This result is somewhat surprising given that the linear plane wave prediction is applicable to wavepackets where the envelope extent is much greater than the wavelength and yet in this case only about 6 wavelengths can be counted across the wavepacket.

The finite-amplitude simulation in Figure 3.2b shows several differences from the small-amplitude simulations. The partially reflected wavepacket in the centre panel has a slightly different structure. The pattern remains crosshatch-like, although the shapes that make up the pattern are now triangular rather than square. There are still heights with no vertical displacement at intervals of $\frac{1}{2}\lambda_z$, however, there are no longer horizontal columns with no vertical displacement. This is likely caused by horizontal phase shifting of the incident and reflected wavepackets due to the presence of a larger wave-induced mean-flow. The right panel shows a significant change in the late-time wavepacket envelopes after interacting with the N^2-barrier. The transmitted wavepacket has an increased vertical spread in the trailing half while the reflected portion shows signs of separating into several distinct wavepackets. The finite-amplitude wavepacket has undergone significant vertical and horizontal dispersion due to nonlinear effects.

The transmission coefficient found in the finite-amplitude simulation is $T = 51.6\%$ which is 22% larger than the small-amplitude simulation and 23% larger than the linear plane wave prediction. This increase in transmission is quite remarkable since these waves have a propagation angle of $\Theta = -45°$ which already has the highest predicted transmission rate.

The differences in wavepacket structure at large amplitudes are partially explained by examining profiles of the wave-induced mean-flow given by (3.10) at various times. Figures 3.3a and 3.3b show the normalized wave-induced mean-flow for the small and finite amplitude simulations examined in Figure 3.2. The left panels are of the initial wave-induced mean-flow given explicitly by (3.12). The middle panels display the largest values of the wave-induced mean-flow during the simulations. This occurs just as the centre of the initial wavepacket reaches the N^2-barrier so that the superposition of the incident and reflected wavepackets generates the largest wave amplitudes. In the small-amplitude case the maximum value is $\mathcal{M}_\sigma = 0.02\, c_{g_x}$ so the effect of self-acceleration is negligible. The maximum value of the finite-amplitude flow is $\mathcal{M}_\sigma = 0.81\, c_{g_x}$ which appears to be large enough that self-acceleration effects begin to cause the divergence of the reflected wavepacket seen at later times.

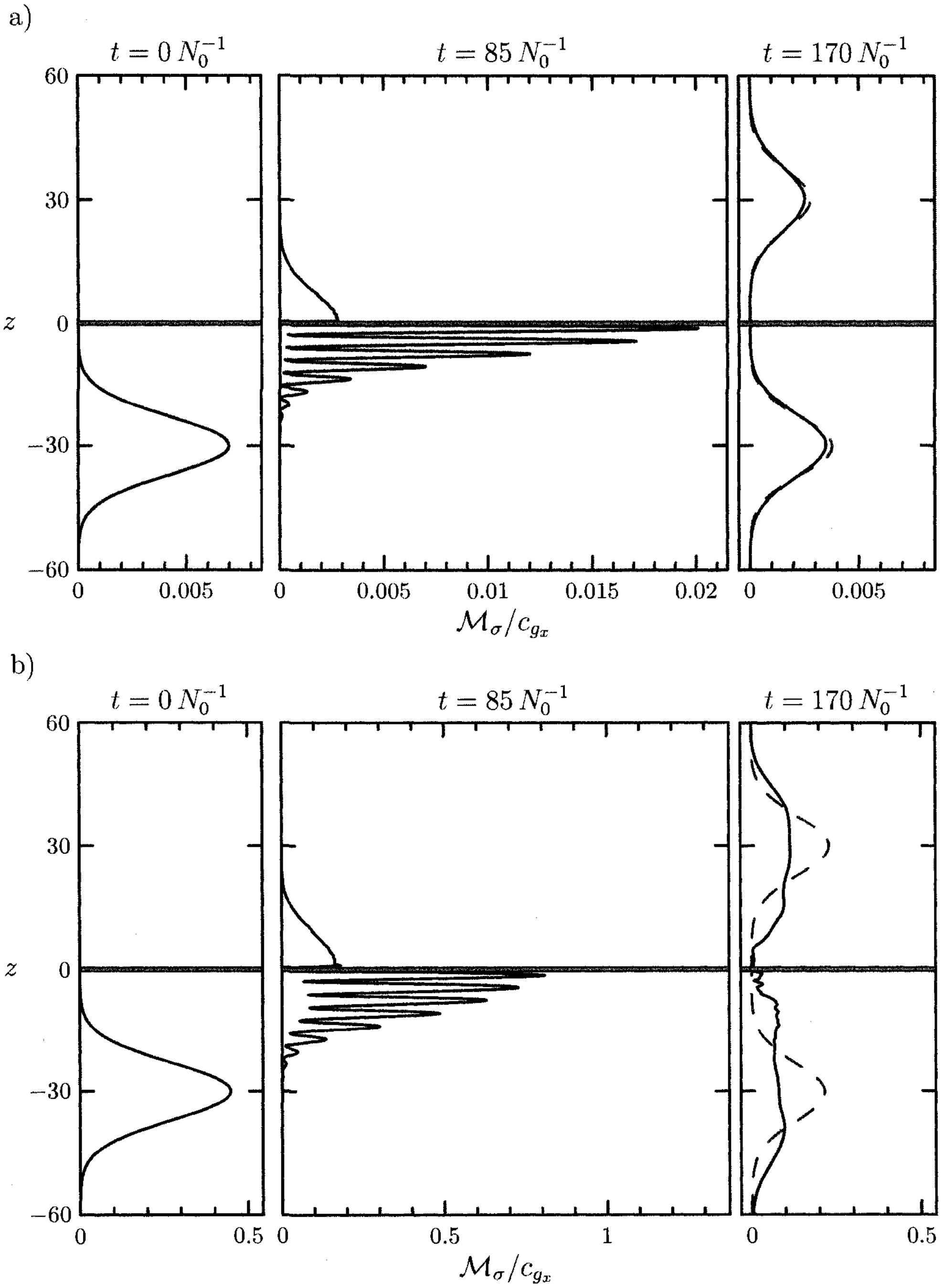

Figure 3.3: The wave-induced mean-flow given by (3.10) at various times for fully nonlinear numerical simulations. The small and large amplitude simulations used in a) and b) respectively are the same as those used in Figure 3.2. The dashed lines in the right panels represent an idealized $\mathcal{M}_\sigma$ if the transmitted and reflected wavepackets retained Gaussian shapes.

One might expect the maximum amplitude of the wave-induced mean-flow in the finite-amplitude case to have increased by a factor equal to the square of the wavepacket amplitude increase, in this case a factor of 64. The maximum amplitude has increased by a smaller factor than this for two reasons. The first is that the transmission coefficient is higher and therefore the reflection coefficient is smaller. The second is that the maximum amplitude of the incident wavepacket has already reduced due to dispersion by the time the wavepacket reaches the barrier. Another important feature of these profiles is the large shear due to the crosshatch pattern of the superimposed wavepackets. This shear is even greater for waves with larger propagation angles and therefore smaller vertical wavelengths.

The right panels of the figure are of the wave-induced mean-flow after the wavepacket has interacted with the N^2-barrier. The dashed lines represent an idealized wave-induced mean-flow calculated as

$$T \cdot \mathcal{M}_\sigma \left(z - c_{g_z} t\right) + R \cdot \mathcal{M}_\sigma \left(-z - c_{g_z} t\right) \tag{3.15}$$

where $\mathcal{M}_\sigma(z)$ is given by (3.12). Comparing this idealized flow with the calculated wave-induced mean-flow in the small amplitude case shows only a slight decrease in the maximum amplitude and a small increase in vertical extent confirming the lack of vertical spread due to linear dispersion. Nonlinear effects clearly enhance the dispersion as evidenced by the finite-amplitude simulation. The vertical extent of the wavepacket envelope has increased and no longer retains a Gaussian shape, although, the leading edges of both the transmitted and reflected wavepackets do appear to have a Gaussian shape. This suggests the increased vertical dispersion due to large-amplitude effects occurs beginning at the centre of the wavepacket where the amplitude is largest.

The late time normalized wave-induced mean-flow for several other vertical wavenumbers is shown in Figure 3.4. The profiles are taken at $t = 190, 155,$

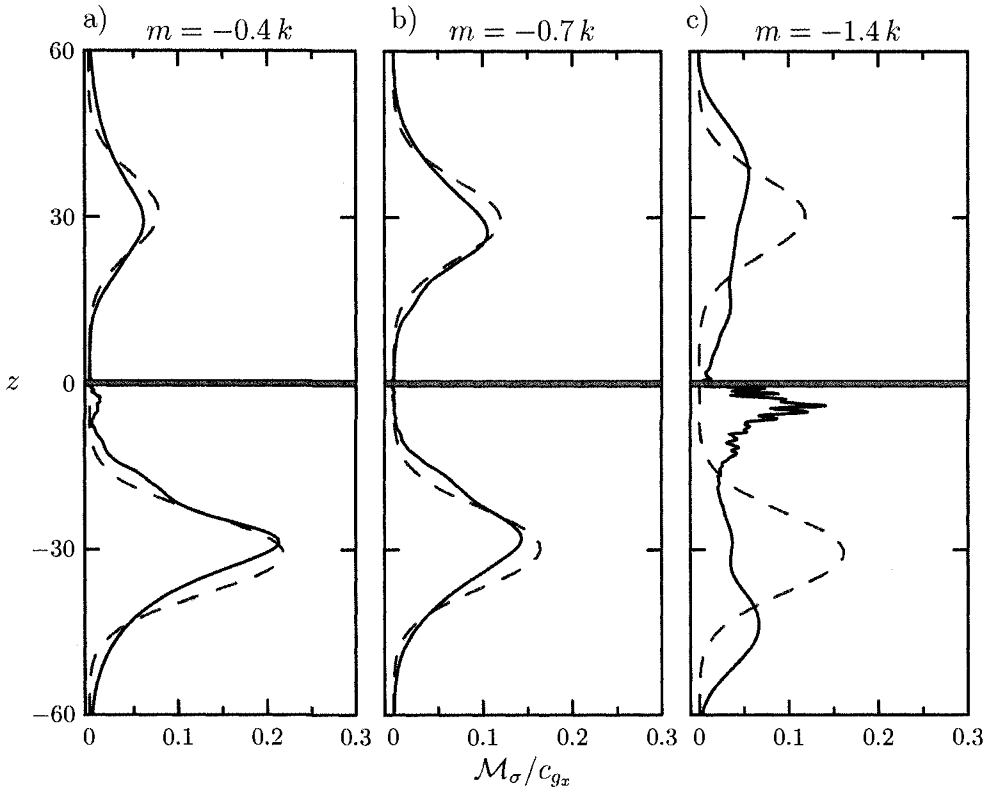

Figure 3.4: The wave-induced mean-flow given by (3.10) at late times for three simulations with varying vertical wavenumbers. Wavepackets are initialized with $A_\xi = 0.045\,\lambda_x$ and $m = -0.4\,k$ in a), $A_\xi = 0.06\,\lambda_x$ and $m = -0.7\,k$ in b), and $A_\xi = 0.06\,\lambda_x$ and $m = -1.4\,k$ in c). In all simulations $\sigma_x = \sigma_z = 10\,k^{-1}$ and $L = 1.0\,k^{-1}$. Profiles are taken at $t = 190, 155, \text{and } 220\,N_0^{-1}$ in a), b), and c) respectively. The dashed lines represent an idealized $\mathcal{M}_\sigma$ were the transmitted and reflected wavepackets Gaussian.

and $220\,N_0^{-1}$ for wavepackets with $m = -0.4, -0.7$, and $-1.4\,k$ in the left, centre, and right panels. The times are chosen so that $c_{g_z} t \approx 6\sigma_z$. Again, the dashed lines show an idealized wave-induced mean-flow given by (3.15). Simulations for wavepackets with $m = -0.4$ and $-0.7\,k$ have transmitted and reflected amplitude envelopes with nearly Gaussian shape centred at heights predicted by linear theory. The peaks of each envelope in these cases is slightly lower and slower moving than the idealized prediction. Each amplitude envelope has broadened due to dispersion although the left panel shows the peak of the reflected wavepacket envelope steepening even though the maximum remains less than that of the idealized flow. This is the same behaviour shown for wavepackets with $m = -0.4\,k$ in a uniformly stratified background. The right panel, with $m = -1.4\,k$ shows qualitatively different behaviour than the other two. The leading portions of the transmitted and reflected amplitude envelopes retain a Gaussian shape although they are faster moving than linearly predicted. The middle and trailing portions of both amplitude envelopes have broadened considerably from the Gaussian. The second peak of the transmitted amplitude envelope directly below the N^2-barrier is likely caused by strong shear in the wave-induced mean-flow during the reflection process. Because the vertical wavelength of waves in this wavepacket is smaller than for waves with $m = -1.0\,k$ the gradient of the flow is even steeper than seen in the centre panels of Figure 3.3 and therefore the shear is larger. The strong shear contributes to the breakup of the reflected wavepacket leaving slower moving portions near the reflection level leading to the second peak in the wave-induced mean-flow (see Figure B.3).

The results of multiple simulations are summarized in Figure 3.5. The plot shows the calculated transmission coefficients normalized by the linearly predicted transmission values for horizontal plane waves plotted against the initial wave amplitude for wavepackets impinging on a N^2-barrier of width $L = 1.0\,k^{-1}$. Each line on the plot represents a different vertical wavenumber, for the solid line $m = -0.4\,k$ ($\Theta = -22°$), for the dotted line $m = -0.7\,k$ ($\Theta = -35°$), for the dashed-dotted line $m = -1.0\,k$ ($\Theta = -45°$), and for the dashed line $m = -1.4\,k$ ($\Theta = -55°$). These values were chosen because Sutherland (2006) showed that for values on either side of the critical value $\Theta = \pm 35°$ large amplitude wavepackets evolve differently as they propagate. The envelope of wavepackets with $\Theta \leq |35°|$ narrows during propagation whereas wavepackets with $\Theta > |35°|$ broaden. Additionally, internal waves that have

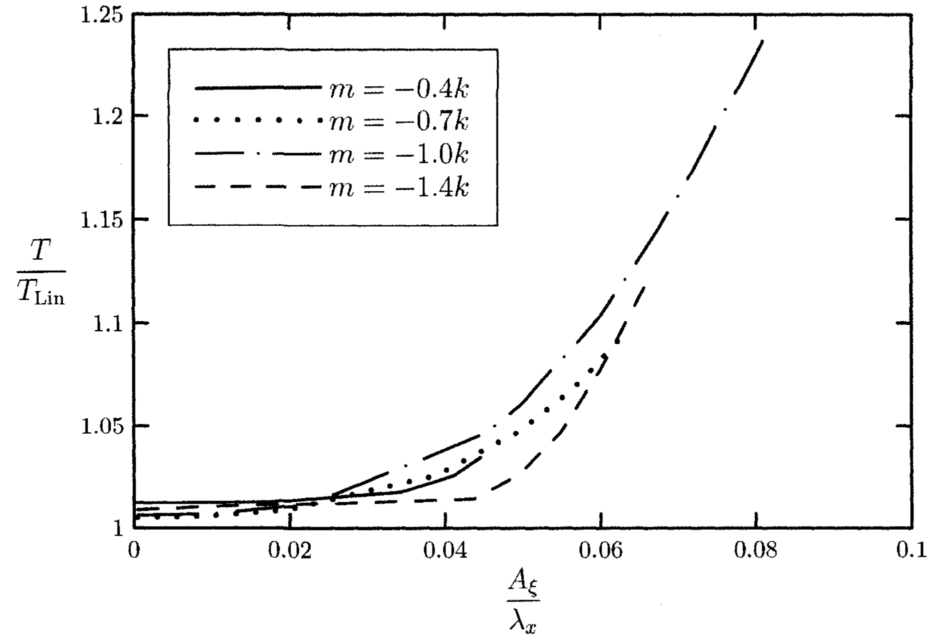

Figure 3.5: Wavepacket transmission values plotted against initial amplitude for horizontally localized wavepackets prescribed initially by (3.2) impinging on a N^2-barrier of width $L = 1.0\,k^{-1}$. The computed transmission values are normalized by the linearly predicted transmission values for horizontal plane waves, T_{Lin}, given by (2.11). Wavepackets are initialized with $\sigma_x = \sigma_z = 10\,k^{-1}$ and $m = -0.4\,k$ (solid line), $m = -0.7\,k$ (dotted line), $m = -1.0\,k$ (dash-dotted line), and $m = -1.4\,k$ (dashed line).

$\Theta = \pm 45^\circ$ are predicted to have the highest transmission rates so higher and lower values were also examined. From the plot we conclude that, regardless of wavenumber, transmission increases as the initial wave amplitude is increased. The increase in transmission is initially quite small for small increases in wave amplitude but for $A_\xi \gtrsim 0.04\,\lambda_x$ the increase is more pronounced. For small wave amplitudes ($A_\xi \lesssim 0.02\,\lambda_x$) all of these curves are within 1.5% of $T/T_{\text{Lin}} = 1$. Wavepackets with $m = -0.4\,k$, where the vertical wavelength is $\lambda_z \approx 16\,k^{-1}$ and $|\sigma_z m| = 40$ is the smallest , have the largest deviation from the linear plane wave prediction at small amplitudes. This suggests that even though wavepackets are compact, plane wave solutions apply in linear cases. Each curve on the plot ends at a different maximum amplitude because beyond some maximum amplitude wavepackets are no longer stable.

3.5.1 Wavepacket extent effects

In addition to amplitude, other initialization parameters of (3.2) are varied to determine the impact on transmission. The effect of the extent of the wavepacket is used to determine how small a wavepacket envelope can be before results significantly deviate from the linear prediction for plane waves. Larger wavepackets require larger domains and therefore longer running times making small wavepackets ideal for this study. Small vertical extents are even more important than small horizontal extents because vertically large wavepackets not only require larger domains but also longer simulations. This is because wavepackets are initially centred $3\sigma_z$ below the N^2-barrier and must run until at least $t = 6\sigma_z/c_{g_z}$ so that the transmitted and reflected portions of the wavepacket clear the barrier. Longer simulation times lead to higher errors from numerical noise as well as having longer running times.

Figure 3.6 shows normalized transmission values calculated using (3.3) plotted against various wavepacket extents for several vertical wavenumbers and an amplitude of $A_\psi = 0.02\, N_0 k^{-2}$ (or $A_\xi \approx 5{\times}10^{-3}\, \lambda_x$). In Figure 3.6a the horizontal extent is varied so that $\sigma_x = 5, 10, 20$, and $40\, k^{-1}$ while $\sigma_z = 10\, k^{-1}$ is kept constant. In Figure 3.6b the vertical extent is varied so that $\sigma_z = 5, 10$, and $15\, k^{-1}$ while $\sigma_x = 10\, k^{-1}$ is kept constant.

The plots show that for wavepackets with σ_x and $\sigma_z \gtrsim 10\, k^{-1}$ the transmission values are within 1% of the linearly predicted values for plane waves. The difference is much larger for σ_x or $\sigma_z = 5\, k^{-1}$. This result justifies the use of $\sigma_x = \sigma_z = 10\, k^{-1}$ in other simulations because the results are consistent with plane wave solutions at small amplitudes. The first plot also shows that for $\sigma_x \lesssim 10\, k^{-1}$ the transmission values are greater than the plane wave predictions whereas for $\sigma_x \gtrsim 20\, k^{-1}$ transmission values are less than plane wave predictions. This is reversed in the second plot where $\sigma_z \lesssim 5\, k^{-1}$ leads to transmission values that are less than the plane wave predictions whereas for $\sigma_z \gtrsim 10\, k^{-1}$ transmission values are greater than plane wave predictions. For small wavepacket extents, normalized transmission values are largest for small $|\sigma_x m|$ and smallest for small $|\sigma_z m|$. For all wavepacket sizes the smallest vertical wavenumber, and thus longest vertical wavelength, leads to the greatest deviation in transmission. For example, the wavepacket with the longest vertical wavelength ($m = -0.7\, k$, $\lambda_z \approx 1.4\, \lambda_x$) has an increase of 2.9% in transmission with $\sigma_x = 5\, k^{-1}$. Note that simulations for wavepackets with $\sigma_x = 40\, k^{-1}$ use an older routine based on energy rather than pseudoenergy to calculate transmission values. This may be the reason for the small increase in the range of transmission values. Simulations with $\sigma_x = 20\, k^{-1}$ and $\sigma_x = 40\, k^{-1}$ are run with larger horizontal domains of $201\, k^{-1}$ and $402\, k^{-1}$ respectively to ensure negligible effects due to the interaction between the leading and trailing edges of the wavepackets.

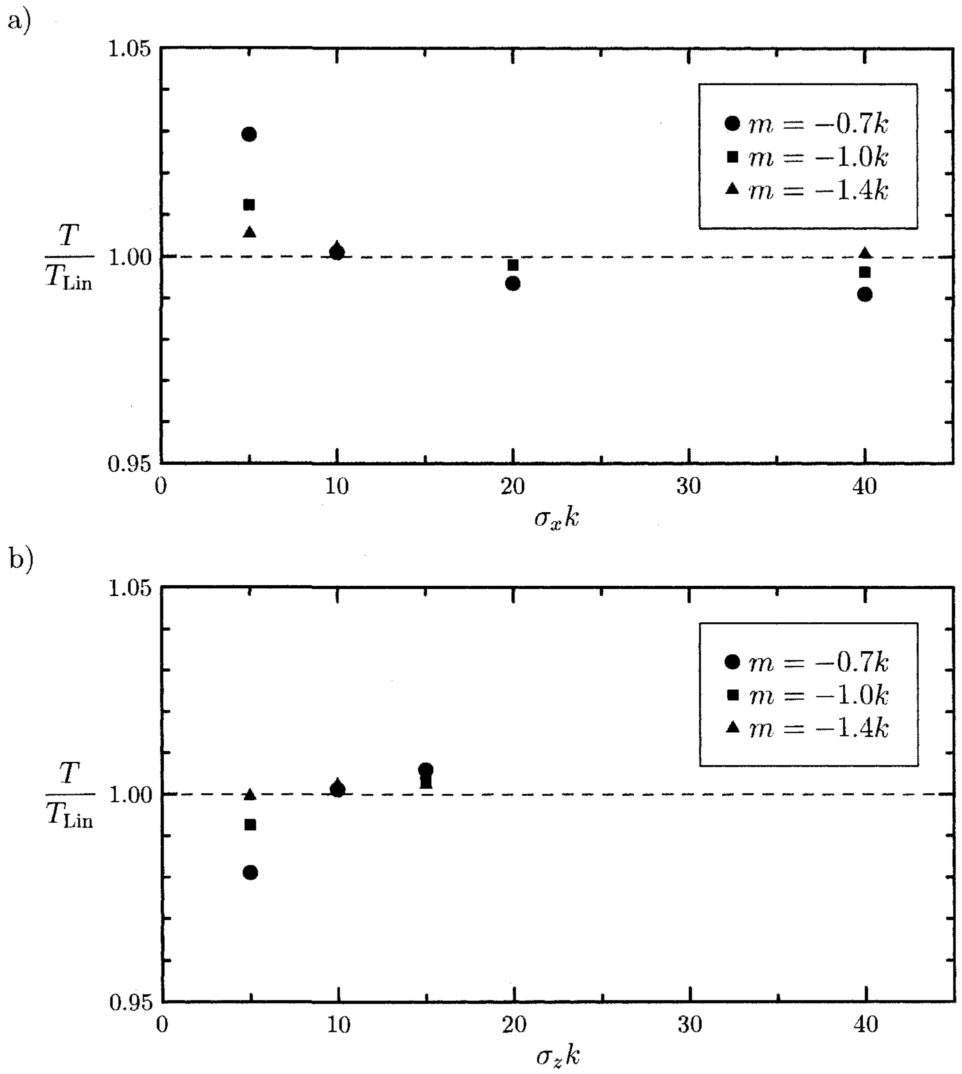

Figure 3.6: Wavepacket transmission values through a N^2-barrier of width $L = 1.0\,k^{-1}$ plotted against the horizontal extent of wavepackets in a) and the vertical extent of wavepackets in b) for several values of the vertical wavenumber, m. Computed transmission values are normalized by the linearly predicted transmission values for horizontal plane waves, T_{Lin}, given by (2.11). Wavepackets are initially prescribed by (3.2) with $A_\psi = 0.02\,N_0 k^{-2}$ (or $A_\xi \approx 5{\times}10^{-3}\,\lambda_x$) and in a) $\sigma_z = 10\,k^{-1}$ while in b) $\sigma_x = 10\,k^{-1}$.

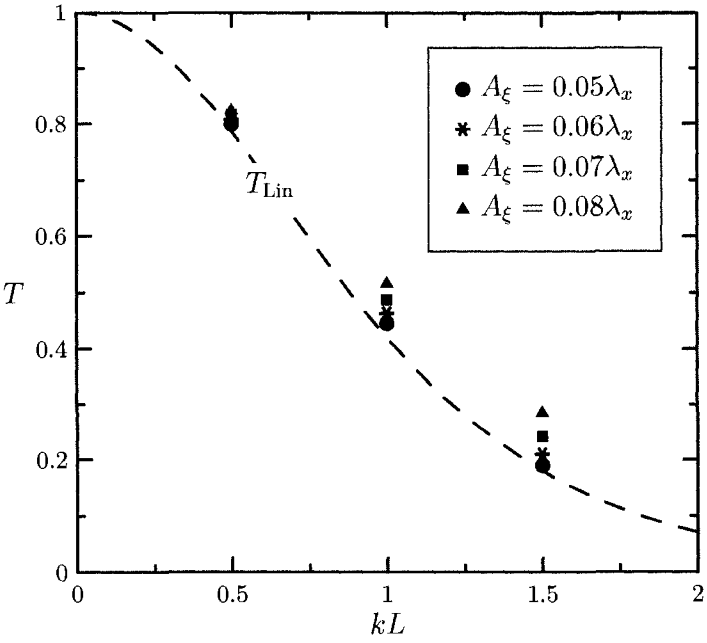

Figure 3.7: Localized wavepacket transmission values plotted against N^2-barrier depths for various initial amplitudes. Wavepackets are initially prescribed by (3.2) with $\sigma_x = \sigma_z = 10\,k^{-1}$ and $m = -1.0\,k$. The dashed line represents the linearly predicted transmission values for horizontal plane waves, T_{Lin}, given by (2.11).

3.5.2 Variations in gap depth

In Chapter 2 two variables, propagation angle, Θ, and gap depth, L, were examined to determine the transmission values. Only propagation angle has been varied in the results of this chapter shown so far while gap depth has been held to a constant $L = 1.0\,k^{-1}$. A number of simulations were run for other values of L that show consistent results with linear predictions. The values of L that were studied were limited by the vertical resolution. For the vertical resolution of $0.05\,k^{-1}$ the smallest gap examined was $L = 0.5\,k^{-1}$ which only resolves 9 vertical levels within the gap. The transmission results for a vertical wavenumber of $m = -1.0\,k^{-1}$ and gap depths of $L = 0.5, 1.0, \text{and } 1.5\,k^{-1}$ are shown in Figure 3.7. Several amplitudes are depicted and show only a small divergence from the linear predictions. Simulations with an amplitude of $A_\xi = 0.08\,\lambda_x$ show the largest increases of 5%, 23%, and 58% in transmission values for gap widths of 0.5, 1.0, and $1.5\,k^{-1}$ respectively. The last value may be incorrect since the maximum wave-induced mean-flow for that simulation is $\mathcal{M}_\sigma = 1.064\,c_{g_x}$ which breaks the self-acceleration condition (3.11). None of the simulations for $A_\xi = 0.07\,\lambda_x$ break the self-acceleration condition and have transmission increases of 4%, 16%, and 34% for gap depths of 0.5, 1.0, and $1.5\,k^{-1}$ respectively. These results are consistent with earlier results that show higher transmission values for larger amplitudes. Although these results show an increase in normalized transmission for smaller gap depths, the actual value of transmission still decreases as gap depths get larger regardless of the initial amplitude. The larger the initial amplitude of a wavepacket the slower the rate at which transmission decreases for larger gap depths.

3.5.3 Horizontal cross-sections

In addition to looking at transmission values for increased initial wavepacket amplitudes, the detailed structure of wavepackets is examined. Horizontal slices of the normalized vertical displacement field are shown in Figure 3.8. The horizontal cross-sections are taken from simulations after running for $t = 85\,N_0^{-1}$ (or $t \approx 13.5\,T_B$) when the centre of the initial wavepacket reaches the N^2-barrier. In Figure 3.8a the initial amplitude is $A_\xi \approx 4.5\times10^{-4}\lambda_x$ whereas in Figures 3.8b and c the initial amplitude is $A_\xi \approx 0.081\,\lambda_x$. The upper panel of each figure is a contour plot that denotes the height of the horizontal slice by a dashed line.

The profiles in both a) and b) are for simulations with $m = -1.0\,k^{-1}$ and are taken at a height of $z = -\frac{3}{8}\lambda_z$ which is below the N^2-barrier in the reflection region. This value is chosen to lie between the heights with the maximum and minimum vertical displacement values. The small-amplitude profile shows

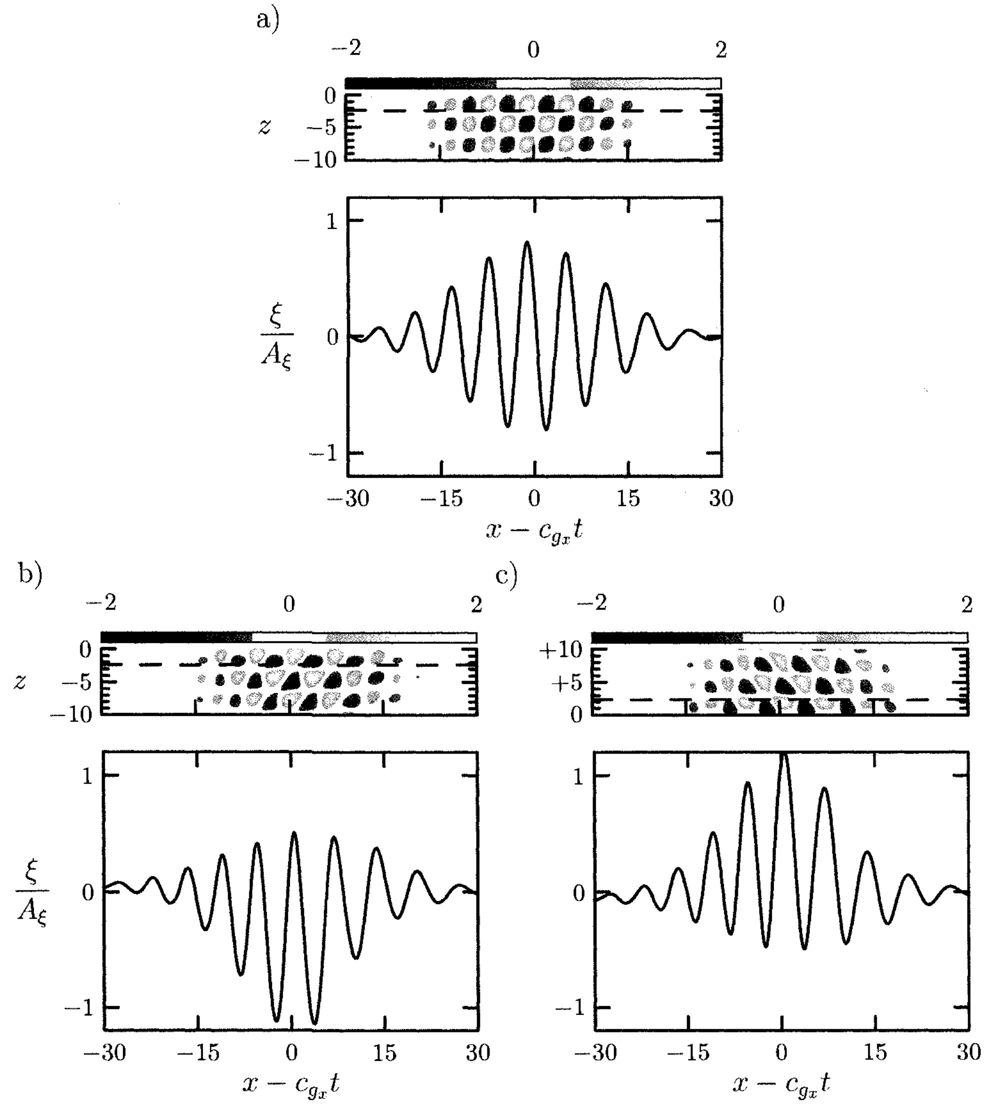

Figure 3.8: Horizontal slices of the normalized vertical displacement field, ξ/A_ξ, at $t = 85\,N_0^{-1}$ for several simulations of a wavepacket impinging on a N^2-barrier of width $L = 1.0\,k^{-1}$. Wavepackets are prescribed by (3.2) with $\sigma_x = \sigma_z = 10\,k^{-1}$.
Profile a) is taken at height $z = -\frac{3}{8}\lambda_z$ for a wavepacket initialized with $A_\xi \approx 4.5{\times}10^{-4}\lambda_x$, $m = -1.0\,k$, and $z_0 = -3\,\sigma_z$.
Profile b) is the same as a) except $A_\xi \approx 0.081\,\lambda_x$.
Profile c) is from a downward propagating wavepacket at height $z = \frac{3}{8}\lambda_z$ with $A_\xi \approx 0.081\,\lambda_x$, $m = 1.0\,k$, and $z_0 = 3\,\sigma_z$.

a wavepacket envelope largely unchanged from an initial Gaussian envelope. The envelope remains symmetric and has a relative maximum vertical displacement of $\xi_{max}/A_\xi = 0.81$ and relative minimum vertical displacement of $\xi_{min}/A_\xi = -0.80$.

The large-amplitude profile in Figure 3.8b have a different wavepacket structure. The peaks of internal waves at this level have broadened and the troughs have steepened. The envelope is no longer symmetric although both the upper and lower halves retain a Gaussian shape. The maximum relative vertical displacement is $\xi_{max}/A_\xi = 0.51$, only 63% of the maximum from the small-amplitude simulation whereas the minimum relative vertical displacement is $\xi_{min}/A_\xi = -1.14$ which is 43% lower than the minimum of the small-amplitude simulation. Slices at different heights exhibit a different structure. For example, a slice through $z = -\frac{5}{8}\lambda_z$ would have steeper peaks and broader troughs.

The behaviour of this large-amplitude internal wavepacket is similar to weakly-nonlinear deep water waves (often called Stokes-waves). The mechanism causing this behaviour, however, is quite different. The steepening of crests and flattening of troughs in deep water waves requires the contribution of waves at larger horizontal wavenumbers (*i.e.* $2k, 3k, \dots$). Such waves are the result of higher order (in amplitude) corrections to a plane wave solution which does not solve the fully non-linear deep water equations that include wave-wave interaction terms. This is not the case for internal waves because plane waves are an exact solution to the fully nonlinear equations (A.13) and so there is no higher order correction. Rather, the influence of nonlinear effects arises due to interactions between the waves and the wave-induced mean-flow. Additionally, simulations of internal wavepackets are Boussinesq (unlike deep water waves), so the only source of directionality that could lead to the non-symmetry of the wavepacket is the initial direction of wavepacket propagation.

To confirm this, a simulation was run with the same large-amplitude initialization as the previously described simulation except that the wavepacket was initially centred $3\,\sigma_z$ above the N^2-barrier rather than below and a positive vertical wavenumber of $m = 1.0\,k$ was used so that the initial direction of propagation was downward. To examine a wavepacket in the reflection region as before, the horizontal slice in Figure 3.8c is taken at $z = \frac{3}{8}\lambda_z$. This wavepacket appears to be a reflection of the other large amplitude wavepacket about $\xi = 0$ confirming the source of the directionality. The structure of internal waves for a downward propagating wavepacket is reversed; peaks are steepened and valleys are broadened.

These changes in wavepacket structure are caused by the large amplitude of the wave-induced mean-flow that occurs between the heights of virtually no vertical displacement. The resulting variable flow Doppler shifts the waves within the incident and reflected wavepackets so that their superposition results in the heightened and reduced advancing and trailing crests. The changes in wavepacket structure at larger initial amplitudes may be a cause of the increased transmission values.

Chapter 4

Summary and Discussion

Internal waves were shown to be able to tunnel through regions of constant density by Sutherland and Yewchuk (2004) who provided analytic predictions of transmission coefficients for various background stratifications. We have extended that work to examine the effect background shear and finite amplitude wavepackets have on transmission.

Using pseudoenergy flux to quantify transmission coefficients, we have derived an analytic prediction for linear internal wave tunnelling across a uniformly mixed shear layer surrounded by stratified fluid. For transmission to occur, the magnitude of the Doppler-shifted frequency of the transmitted waves must be less than the buoyancy frequency in the transmission region. Additionally, the phase speed of incident waves cannot match the flow speed beyond the shear region. For weak shear, maximum transmission occurs for waves with $\omega = N_0/\sqrt{2}$ (equal horizontal and vertical wavenumbers). For stronger shear, waves can transmit across a critical level (where the wave speed matches the background flow speed) if the buoyancy frequency is zero at the critical level and therefore waves are evanescent. The presence of density jumps in the background profile serves to enhance transmission when no critical level is reached, but inhibits transmission across critical levels.

To study the effect amplitude has on internal wave tunnelling numerical simulations of compact wavepackets were run. Using both the spatially integrated pseudoenergy and the time integrated pseudoenergy flux to quantify time dependent transmission coefficients, we have found the transmission values of internal wavepackets at late times for finite-amplitude internal wavepackets tunnelling across a constant density layer surrounded by stratified fluid. A theoretical maximum amplitude for Gaussian wavepackets in which the maximum value of the wave-induced mean-flow within the wavepacket remains less than the horizontal group velocity was determined to be $\frac{A_\xi}{\lambda_x} \lesssim 0.12|\sin 2\Theta|$. For tunnelling wavepackets this maximum amplitude is reduced by as much as half due to the superposition of incident and reflected waves. Wavepackets with amplitudes exceeding this maximum value were found to break apart and diverge due to self-acceleration effects. Small-amplitude wavepackets were found to have only minor changes in wavepacket extent during the course of tunnelling due to linear dispersion. The transmission values were found to be within 1.5% of plane wave predictions for wavepackets with extents as small as $\sigma_x = \sigma_z \geq 10\,k^{-1}$ for all values of the vertical wavenumber. Finite-amplitude wavepackets with amplitudes approaching the theoretical maximum have significantly increased horizontal and vertical dispersion due to nonlinear effects. Transmission values increase significantly for larger initial amplitude wavepackets at all vertical wavenumbers. The increase is as much as 25% for wavepackets tunnelling through a constant density layer of $kL = mL = 1.0$. We found the transmission coefficient for large-amplitude wavepackets decreases at a slower rate than for linear plane waves as the thickness of the constant density layer was increased. The reason for the increase in transmission values at large amplitudes remains unknown although the change in structure of reflecting wavepackets interacting with a highly sheared wave-induced mean-flow profile may provide some insight.

The theories developed in this project can be applied to make *a priori* estimates of internal wave transmission through unstratified layers where the vertical scale of variations in the background is smaller than or comparable to the vertical scale of internal waves. Consider an atmospheric example where wavepackets generated by a storm tunnel through an evanescent region in the mesosphere to reach the ionosphere. If we assume the Boussinesq approximation captures the leading-order dynamics of tunnelling waves then (2.30) can provide a crude estimate of the transmission values. In this example we characterize the buoyancy frequency using the piecewise-linear profile (2.9) with $N_0 \simeq 2.2 \times 10^{-2}\, s^{-1}$ and the background shear assuming that the wind speed increases by $U_0 \simeq 11\, m/s$ over the evanescent region of depth $L = 5\, km$. For waves with horizontal wavelength $\lambda_x \simeq 15\, km$ ($k \simeq 4.2 \times 10^{-4} m^{-1}$) and a period of $390\, s$ ($\omega \simeq 1.6 \times 10^{-2}\, s^{-1}$) we find the following non-dimensional variables: Ri $\simeq$ 100, $\Theta \simeq 43°$, $\Phi \simeq 58.5°$, and $kL \simeq 2.1$. The resulting transmission coefficient is $T \simeq 0.05$. Because the atmosphere is anelastic and not Boussinesq, the amplitude of waves will increase as they propagate upward. This means that a wave with $A_\xi = 0.005\, \lambda_x$ will have an amplitude of $A_\xi = 0.1\, \lambda_x$ after propagating three density scale heights. It would be reasonable to assume that the estimate of T is low because we have seen that larger wave amplitudes lead to higher transmissions. Estimates using these theories are possibly better suited to the ocean where the Boussinesq approximation is valid. Consider a background profile in the ocean with the average buoyancy frequency in both the seasonal and permanent thermocline of $N_0 \simeq 5 \times 10^{-3}\, s^{-1}$, a gap in between of $L \simeq 100\, m$ where waves are evanescent over which the velocity of the background currents increase by $U_0 \simeq 0.1\, m/s$. We can estimate the fraction of pseudoenergy transmitted by internal waves with frequency $\omega \simeq 4 \times 10^{-3}\, s^{-1}$ and horizontal wavelength $\lambda_x \simeq 630\, m$ ($k \simeq 0.01\, m^{-1}$) from the seasonal to the permanent thermocline. Using these values we find the following non-dimensional variables: Ri $\simeq$ 25,

$\Theta \simeq 37^\circ$, $\Phi \simeq 53^\circ$, and $kL \simeq 1$. The transmission coefficient is estimated to be $T \simeq 0.41$. If instead $L \simeq 300\,m$ then $\mathrm{Ri} \simeq 225$ (for the same velocity increase, U_0) and the transmission value would be significantly decreased to $T \simeq 0.01$. These estimates are highly idealized. A more accurate estimate would use measured profiles of the background buoyancy frequency and horizontal velocity rather than an approximate piecewise-linear profile. Nault and Sutherland (2007) have recently developed a numerical method to accomplish this. The results of this thesis were critical in the development of their numerics. The results provided a test case to ensure the numerical method was providing accurate predictions.

In these examples energy is transported away from the original source at a different rate than would be predicted by a heuristic application of ray theory. A future avenue of this research could be to parameterize the effects of internal wave tunnelling to be included in numerical weather models so that energy transport is more accurately represented.

Bibliography

Andrews, D. G. and M. E. McIntyre (1976). Planetary waves in horizontal and vertical shear: The generalized Eliassen-Palm relation and the mean flow acceleration. *J. Atmos. Sci. 33*, 2031–2048.

Andrews, D. G. and M. E. McIntyre (1978). On wave action and its relatives. *J. Fluid Mech. 89*, 647–664.

Bretherton, F. P. (1966). Gravity waves in shear. *Quart. J. Roy. Meteorol. Soc. 92*, 466–480.

Broutman, D., J. W. Rottman, and S. D. Eckermann (2004). Ray methods for internal waves in the atmosphere and ocean. *Annu. Rev. Fluid Mech. 36*, 233–253.

Brown, G. L. and B. R. Sutherland (2007). Internal wave tunnelling through non-uniformly stratified shear flow. *Atmos. Ocean 45*, 47–56.

Drazin, P. G. and W. H. Reid (1981). *Hydrodynamic Stability.* Cambridge, England: Cambridge University Press.

Eckart, C. (1961). Internal waves in the ocean. *Phys. Fluids 4*, 791–799.

Eliassen, A. and E. Palm (1961). On the transfer of energy in stationary mountain waves. *Geofys. Publ. 22*, 1–23.

Fritts, D. C. and L. Yuan (1989). An analysis of gravity wave ducting in the atmosphere: Eckart's resonances in thermal and Doppler ducts. *J. Geophys. Res. 94*(D15), 18455–18466.

Ledwell, J. R., E. Montgomery, K. Polzin, L. C. St.Laurent, R. Schmitt, and J. Toole (2000). Evidence for enhanced mixing over rough topography in the abyssal ocean. *Nature 403*, 179–182.

Lighthill, M. J. (1978). *Waves in Fluids.* Cambridge, England: Cambridge University Press.

Lindzen, R. S. and K.-K. Tung (1976). Banded convective activity and ducted gravity waves. *Mon. Wea. Rev. 104*, 1602–1617.

McFarlane, N. A. (1987). The effect of orographically excited gravity wave drag on the general circulation of the lower stratosphere and troposphere. *J. Atmos. Sci. 44*, 1775–1800.

McLandress, C. (1998). On the importance of gravity waves in the middle atmosphere and their parameterization in general circulation models. *J. Atmos. Sol.-Terres. Phys. 60*, 1357–1383.

Nault, J. T. and B. R. Sutherland (2007). Internal wave transmission in nonuniform flows. *Physics of Fluids 19*(1), 016601.

Polzin, K. L., J. M. Toole, J. R. Ledwell, and R. W. Schmitt (1997). Spatial variability of turbulent mixing in the Abyssal Ocean. *Science 276*, 93–96.

Scinocca, J. F. and T. G. Shepherd (1992). Nonlinear wave-activity conservation laws and Hamiltonian structure for the two-dimensional anelastic equations. *J. Atmos. Sci. 49*, 5–27.

Skyllingstad, E. D. and D. W. Denbo (1994). The role of internal gravity waves in the equatorial current system. *J. Phys. Oceanogr. 24*, 2093–2110.

Sutherland, B. R. (2001). Finite-amplitude internal wavepacket dispersion and breaking. *J. Fluid Mech. 429*, 343–380.

Sutherland, B. R. (2006). Weakly nonlinear internal gravity wavepackets. *J. Fluid Mech. 569*, 249–258.

Sutherland, B. R. and W. R. Peltier (1994). Turbulence transition and internal wave generation in density stratified jets. *Phys. Fluids A 6*, 1267–1284.

Sutherland, B. R. and K. Yewchuk (2004). Internal wave tunnelling. *J. Fluid Mech. 511*, 125–134.

Wang, T.-A. and Y.-L. Lin (1999). Wave ducting in a statified shear flow over a two-dimensional mountain. part 1: General linear criteria. *J. Atmos. Sci. 56*, 412–436.

Appendix A

Internal Gravity Wave Theory

A.1 Equations of Fluid Motion

The governing equations of fluid motion used in most circumstances, including the motion of internal waves, are the Navier-Stokes equation

$$\varrho \frac{\mathrm{D}\boldsymbol{u_T}}{\mathrm{D}t} = -\boldsymbol{\nabla} P + \varrho \boldsymbol{g} + \mu \left(\boldsymbol{\nabla}^2 \boldsymbol{u_T} + \frac{1}{3} \boldsymbol{\nabla} \left(\boldsymbol{\nabla} \cdot u_T \right) \right), \tag{A.1}$$

representing the conservation of momentum, and the continuity equation

$$\frac{\partial \varrho}{\partial t} + \boldsymbol{\nabla} \cdot (\varrho \boldsymbol{u_T}) = 0, \tag{A.2}$$

representing the conservation of mass. In these equations ϱ is the total density of the fluid, P is the total pressure, $\boldsymbol{g} = -g\hat{\boldsymbol{z}}$ is the acceleration due to gravity, μ is the molecular viscosity, and $\boldsymbol{u_T} = U\hat{\boldsymbol{x}} + V\hat{\boldsymbol{y}} + W\hat{\boldsymbol{z}}$ is the velocity field. The *material derivative*,

$$\frac{\mathrm{D}}{\mathrm{D}t} \equiv \frac{\partial}{\partial t} + \boldsymbol{u_T} \cdot \boldsymbol{\nabla}, \tag{A.3}$$

is the total rate of change following a fluid element in which $\frac{\partial}{\partial t}$ is the local rate of change of the fluid at a given point and the *advective derivative*, $\boldsymbol{u_T} \cdot \boldsymbol{\nabla}$, is the change as the result of the advection of a fluid element from one location to another. The advective terms of the material derivative are the source of nonlinearity in the equations of motion.

To simplify these equations, several assumptions are made. If the fluid is incompressible then the total density cannot change following the motion, which gives

$$\frac{\mathrm{D}\varrho}{\mathrm{D}t} = 0. \tag{A.4}$$

This assumption together with the continuity equation (A.2) gives the condition

$$\boldsymbol{\nabla} \cdot \boldsymbol{u_T} = 0. \tag{A.5}$$

This assumption is good for the ocean and is reasonable for the atmosphere if the vertical scales of motion are less than a density scale height, on the order of 10 km. If we further assume the fluid is inviscid, then we can set $\mu = 0$ which reduces (A.1) to the Euler equation,

$$\varrho \frac{\mathrm{D}\boldsymbol{u_T}}{\mathrm{D}t} = -\boldsymbol{\nabla} P + \varrho \boldsymbol{g}. \tag{A.6}$$

For large-scale flows in the atmosphere and ocean Reynolds numbers (the ratio of inertial forces to viscous forces) are large and this approximation is valid. To further simplify the governing equations, we decompose the pressure and density fields as

$$\begin{aligned} P(\boldsymbol{x}, t) &= \bar{P}(z) + p(\boldsymbol{x}, t) \\ \varrho(\boldsymbol{x}, t) &= \bar{\rho}(z) + \rho(\boldsymbol{x}, t), \end{aligned} \tag{A.7}$$

where $\bar{P}(z)$ and $\bar{\rho}(z)$ are background fields that vary only in the vertical and $p(\boldsymbol{x}, t)$ and $\rho(\boldsymbol{x}, t)$ are perturbation fields. The amplitude of variations of the perturbation fields are much less those of the background. We now assume that the background pressure and density are in hydrostatic balance, which is the statement that the pressure at any vertical level is due to the weight of the column of fluid above that level. It can be written as

$$\bar{P}(z) = P_0 - g \int_{z_0}^{z} \bar{\rho}\left(\tilde{z}\right) \, \mathrm{d}\tilde{z} \tag{A.8a}$$

where P_0 is a constant reference pressure at a reference height, z_0. This balance is more commonly expressed in terms of derivatives as

$$\frac{\mathrm{d}\bar{P}}{\mathrm{d}z} = -g\bar{\rho}. \tag{A.8b}$$

Finally, we make the Boussinesq approximation which means that density variations are only relevant to the momentum equation (A.1) as they effect the buoyancy term, $\varrho \boldsymbol{g}$. To make this approximation we write $\bar{\rho}(z) = \rho_0 \left[1 + \varepsilon r(z)\right]$ where ρ_0 is a characteristic density, $r(z)$ is the non-dimensional background density of maximum order unity, ε is the ratio of the change of density to the characteristic density, and we assume that $\varepsilon \ll 1$. The result of these approximations turns (A.4) and (A.6) into

$$\rho_0 \frac{\mathrm{D}\boldsymbol{u_T}}{\mathrm{D}t} = -\boldsymbol{\nabla} p + \rho \boldsymbol{g} \tag{A.9a}$$

$$\frac{\mathrm{D}\rho}{\mathrm{D}t} + W \frac{\mathrm{d}\bar{\rho}}{\mathrm{d}z} = 0 \tag{A.9b}$$

which, together with (A.5), are called the Boussinesq equations. It is often convenient to rewrite the $\frac{\mathrm{d}\bar{\rho}}{\mathrm{d}z}$ term of equation (A.9b) in terms of the buoyancy frequency. Explicitly, under the Boussinesq approximation, the buoyancy frequency, N, is defined as

$$N^2(z) = -\frac{g}{\rho_0} \frac{\mathrm{d}\bar{\rho}}{\mathrm{d}z}. \tag{A.10}$$

In this study we are primarily interested in motions in the $x - z$ plane and thus we set the velocity and all variations in the $\hat{\boldsymbol{y}}$ direction to be zero, *i.e.* $V = 0$ and $\frac{\partial}{\partial y} \to 0$. Substituting $\boldsymbol{u_T} = \bar{U}(z)\hat{\boldsymbol{x}} + \boldsymbol{u}(\boldsymbol{x}, t)$, where $\bar{U}(z)$ is the background horizontal flow, and $\boldsymbol{u} = u\hat{\boldsymbol{x}} + w\hat{\boldsymbol{z}}$, the perturbation velocity, the momentum equations become

$$\rho_0 \left(\frac{\mathrm{D}u}{\mathrm{D}t} + w\bar{U}' \right) = -\frac{\partial p}{\partial x} \tag{A.11a}$$

$$\rho_0 \frac{\mathrm{D}w}{\mathrm{D}t} = -\frac{\partial p}{\partial z} - g\rho. \tag{A.11b}$$

By restricting the flow to two-dimensions, condition (A.5) now implies that the two remaining components of $\boldsymbol{u}$ can be determined from a scalar function, ψ, known as the *streamfunction*. The streamfunction is defined so that $\boldsymbol{u} = \boldsymbol{\nabla} \times (\psi \hat{\boldsymbol{y}})$, or explicitly

$$u = -\frac{\partial \psi}{\partial z} \quad \text{and} \quad w = \frac{\partial \psi}{\partial x}. \tag{A.12}$$

Pressure can be eliminated can be from the governing equations by taking the curl of the momentum equations (A.11) and applying (A.5). This reduces the governing equations to the following set of coupled equations

$$\frac{\mathrm{D}\zeta}{\mathrm{D}t} = \frac{g}{\rho_0}\frac{\partial \rho}{\partial x} - \bar{U}''\frac{\partial \psi}{\partial x} \tag{A.13a}$$

$$\frac{g}{\rho_0}\frac{\mathrm{D}\rho}{\mathrm{D}t} = N^2\frac{\partial \psi}{\partial x} \tag{A.13b}$$

Which are written in terms of the unknown variables ρ, ψ, and ζ. The last of these is the vorticity, ζ, defined as the curl of velocity

$$\zeta \equiv (\boldsymbol{\nabla} \times \boldsymbol{u}) \cdot \hat{\boldsymbol{y}} \equiv -\boldsymbol{\nabla}^2\psi. \tag{A.14}$$

A.2 Linearization

If we make the final simplifying assumption that the amplitude of perturbations are small, then the nonlinear terms in the governing equations may be neglected. In particular the material derivative becomes $\frac{\mathrm{D}}{\mathrm{D}t} \rightarrow \frac{\partial}{\partial t} + \bar{U}\frac{\partial}{\partial x}$. Applying the small amplitude assumption the coupled equations (A.13a) and (A.13b) can be reduced to a single governing equation:

$$\frac{\mathrm{D}^2}{\mathrm{D}t^2}\left(\boldsymbol{\nabla}^2\psi\right) - \bar{U}''(z)\frac{\mathrm{D}}{\mathrm{D}t}\left(\frac{\partial \psi}{\partial x}\right) + N^2(z)\frac{\partial^2 \psi}{\partial x^2} = 0. \tag{A.15}$$

Because all coefficients of (A.15) are independent of x and t and assuming the domain is horizontally unbounded, solutions are of the form

$$\psi(x, z, t) = \phi(z)e^{i(kx-\omega t)} + \text{c.c.} \tag{A.16}$$

where k is a horizontal wavenumber, ω is an (absolute) frequency, and $\phi(z)$, is the streamfunction amplitude (possibly complex) which depends on height. This form of the solution reduces the partial differential equation (A.15) to an ordinary differential equation

$$\phi''(z) + k^2\left(\frac{N^2(z)}{\bar{\Omega}^2(z)} + \frac{\bar{U}''(z)}{k\bar{\Omega}(z)} - 1\right)\phi(z) = 0, \tag{A.17}$$

known as the Taylor-Goldstein equation. In this formula $\bar{\Omega}$ is the relative (or Doppler-shifted) frequency, given by

$$\bar{\Omega}(z) = \omega - k\bar{U}(z). \tag{A.18}$$

The Taylor-Goldstein equation can be used to study the stability of parallel shear flows and internal wave tunnelling.

A.3 Dispersion Relation

For a uniformly stratified fluid, N^2 is constant. If additionally the background flow has no shear (*i.e.* $\bar{U}(z) = U_0$) then $\bar{U}'' = 0$ and equation (A.15) reduces to

$$\left(\frac{\mathrm{D}^2}{\mathrm{D}t^2}\nabla^2 + N^2\frac{\partial^2}{\partial x^2}\right) b = 0. \tag{A.19}$$

Because of the simplifications the function $b(\boldsymbol{x}, t)$ can now be any field of the same order as the streamfunction (*i.e.* $u, w, \rho, p \ldots$). Again if the domain is unbounded solutions are of the form

$$b(x, z, t) = A_b e^{i(kx+mz-\omega t)} + \text{c.c.}, \tag{A.20}$$

where k and ω are defined as before and m is a vertical wave number. For non-trivial solutions where $A_b \neq 0$ the dispersion relation for non-steady solutions found from (A.19) is

$$\Omega^2 = \frac{N^2 k^2}{k^2 + m^2} \tag{A.21}$$

where the relative frequency, $\Omega = \omega - kU_0$, is now constant. Taking the square root of both sides, the frequency is found explicitly to be

$$\Omega = \pm N\frac{k}{|\boldsymbol{k}|} \text{ or } \omega = k\left(U_0 \pm \frac{N}{|\boldsymbol{k}|}\right) \tag{A.22}$$

where $\boldsymbol{k} = (k, m)$ is the total wavenumber vector. It is conceptually convenient to require that ω is positive so that the direction of wave propagation is determined by the wavenumber vector. In particular, the horizontal phase speed, $c = \omega/k$ is determined by the sign of the horizontal wavenumber. To ensure the frequency is positive, the plus/minus sign in (A.22) is positive if $c > U_0$ and negative if $c < U_0$. An immediate consequence of the dispersion relation is that the frequency of propagating internal waves cannot exceed the buoyancy frequency. Disturbances with relative frequencies $|\Omega| > N$ decay exponentially and are called *evanescent waves.*

In the circumstance where $U_0 = 0$, it is often more convenient to represent the dispersion relation in terms of the angle between $\boldsymbol{k}$ and k defined as

$$\Theta \equiv \tan^{-1}\left(\frac{m}{k}\right) \tag{A.23}$$

in which case the dispersion relation (A.22) becomes

$$\omega = N\cos\Theta. \tag{A.24}$$

In real space Θ is the angle between lines of constant phase and the z-axis. To ensure ω is positive we require that $-90° \leq \Theta \leq 90°$.

A.4 Properties of Linear Internal Waves

A wave field that is particularly useful to describe physical properties is the vertical displacement, ξ, defined in terms of the perturbation and the background density as

$$\xi \equiv \frac{\rho}{-\frac{\mathrm{d}\bar{\rho}}{\mathrm{d}z}} = \frac{g}{\rho_0 N^2}\rho. \tag{A.25}$$

For small amplitude waves the vertical displacement can also be found implicitly through the relation

$$\frac{\mathrm{D}\xi}{\mathrm{D}t} = w \tag{A.26}$$

which is the statement that the rate of change of vertical displacement with time is the vertical velocity. If ξ and w are in the form of (A.20) then the

Table A.1: Relations between linear fields and the vertical displacement field.

Field variable: b	Amplitude: A_b	A_b for $U_0 = 0$
ξ	A_ξ	A_ξ
$w = \frac{\mathrm{D}\xi}{\mathrm{D}t}$	$A_w = -i\Omega A_\xi$	$A_w = -iN\cos\Theta A_\xi$
$\frac{\partial\psi}{\partial x} = w$	$A_\psi = -\frac{\Omega}{k} A_\xi$	$A_\psi = -\frac{N}{k}\cos\Theta A_\xi$
$u = -\frac{\partial\psi}{\partial z}$	$A_u = i\Omega\frac{m}{k} A_\xi$	$A_u = iN\sin\Theta A_\xi$
$\zeta = -\nabla^2\psi$	$A_\zeta = -N^2\frac{k}{\Omega} A_\xi$	$A_\zeta = -Nk\sec\Theta A_\xi$
$\rho = -\frac{\mathrm{d}\bar{\rho}}{\mathrm{d}z}\xi$	$A_\rho = \frac{\rho_0}{g} N^2 A_\xi$	$A_\rho = \frac{\rho_0}{g} N^2 A_\xi$
$\frac{\partial p}{\partial x} = -\rho_0\frac{\mathrm{D}u}{\mathrm{D}t}$	$A_p = i\rho_0\Omega^2\frac{m}{k^2} A_\xi$	$A_p = i\rho_0\frac{N^2}{k}\cos\Theta\sin\Theta A_\xi$

complex amplitude of vertical velocity in terms of the amplitude of vertical displacement is $A_w = -i\Omega A_\xi$. Other polarization relations of basic state fields can found in terms of A_ξ from the governing equations. These are summarized in Table A.1. These relations can be written in several forms using the dispersion relation and can be determined if the basic field amplitude and two of ω, k, m, or Θ are known.

The velocities at which waves propagate can be determined if the frequency and wavenumber are specified. The phase velocity is the speed and direction at which lines of constant phase move. Under this definition the phase velocity is

$$\boldsymbol{c_p} \equiv \frac{\omega}{|\boldsymbol{k}|}\frac{\boldsymbol{k}}{|\boldsymbol{k}|} = \frac{\omega}{k^2+m^2}\,(k, m)\,. \tag{A.27}$$

Moving in a frame of reference with the background (*i.e.* $U_0 = 0$) the phase velocity of internal waves is

$$\boldsymbol{c_p} = \frac{N|k|}{|\boldsymbol{k}|^3}\,(k, m)\,. \tag{A.28}$$

Written in terms of Θ, the horizontal component of the phase velocity is

$$c_{p_x} = \frac{N}{|\boldsymbol{k}|}\mathrm{sign}(k)\cos^2\Theta = \frac{N}{k}\cos^3\Theta \tag{A.29a}$$

and the vertical component is

$$c_{p_z} = \frac{N}{|\boldsymbol{k}|}\cos\Theta\sin\Theta = \frac{N}{|k|}\cos^2\Theta\sin\Theta. \tag{A.29b}$$

The group velocity is the velocity of a wavepacket and the velocity of energy transport. It is defined as

$$\boldsymbol{c_g} \equiv \left(\frac{\partial\omega}{\partial k}, \frac{\partial\omega}{\partial m}\right). \tag{A.30}$$

Again, moving in a frame of reference with the background, the group velocity of internal waves is

$$\boldsymbol{c_g} = \frac{N|k|}{|\boldsymbol{k}|^3}\left(\frac{m^2}{k}, -m\right). \tag{A.31}$$

Written in terms of Θ, the horizontal component of the group velocity is

$$c_{g_x} = \frac{N}{|\boldsymbol{k}|}\mathrm{sign}(k)\sin^2\Theta = \frac{N}{k}\cos\Theta\sin^2\Theta \tag{A.32a}$$

and the vertical component is

$$c_{g_z} = -\frac{N}{|\boldsymbol{k}|}\cos\Theta\sin\Theta = -\frac{N}{|k|}\cos^2\Theta\sin\Theta. \tag{A.32b}$$

An interesting property of internal waves is that $\boldsymbol{c_g} \cdot \boldsymbol{c_p} = 0$, meaning that the phase and group velocity are at right angles or, equivalently, that the group velocity is directed along lines of constant phase. In particular, waves with $k > 0$ and $m < 0$ have a phase velocity oriented downward and to the right and a group velocity upward and to the right. Another property is that the vertical group velocity is zero for $\Theta = 0°$ and $\Theta = \pm 90°$ and is maximized when k is fixed for $\Theta = \tan^{-1}\left(\pm\frac{1}{\sqrt{2}}\right) \simeq \pm 35°$, or equivalently $m = \pm\frac{k}{\sqrt{2}}$. We note that when $U_0 \neq 0$ applying (A.30) to (A.22) gives a shifted horizontal group velocity of

$$c_{g_x} = \frac{N|k|m^2}{|\boldsymbol{k}|^3 k} + U_0. \tag{A.33}$$

A.5 Pseudoenergy

Wave energy, or the flux of wave energy, is a property of internal waves that is often used to characterize internal wave motions. For the tunnelling problem, the flux of wave energy is particularly useful to quantify the transmission of internal waves through a barrier. A relation between wave energy and the flux of wave energy defined in the classical sense can be derived directly from the fully nonlinear equations of motion. We begin by adding the product of the horizontal momentum equation (A.11a) and the horizontal velocity of the disturbance, u, to the product of the vertical momentum equation (A.11b) and the vertical velocity of the disturbance, w, and applying (A.5) to find

$$\frac{\partial E_k}{\partial t} + \boldsymbol{\nabla} \cdot \left[\boldsymbol{u}\left(p + E_k\right) + \hat{\boldsymbol{x}}\bar{U}E_k\right] = -g\rho w - \rho_0 uw\bar{U}' \tag{A.34}$$

where

$$E_k = \frac{1}{2}\rho_0\left(u^2 + w^2\right) \tag{A.35}$$

is the kinetic energy of the disturbance. Next, if the stratification is constant, equation (A.13b) is multiplied by $g\rho$ and (A.5) is applied to find

$$\frac{\partial E_p}{\partial t} + \boldsymbol{\nabla} \cdot \left(\boldsymbol{u}E_p + \hat{\boldsymbol{x}}\bar{U}E_p\right) = g\rho w \tag{A.36}$$

where

$$E_p = \frac{1}{2}\frac{g^2\rho^2}{\rho_0 N^2} = \frac{1}{2}\rho_0\left(N^2\xi^2\right) \tag{A.37}$$

is the available potential energy of the disturbance. Adding (A.34) to (A.36) gives the energy equation

$$\frac{\partial E}{\partial t} + \boldsymbol{\nabla} \cdot \left[\boldsymbol{u}\left(p + E\right) + \hat{\boldsymbol{x}}\bar{U}E\right] = -\rho_0 uw\bar{U}' \tag{A.38}$$

where the wave energy, E is the sum of the kinetic and available potential wave energies. We see from (A.38) that energy changes in time not only due to the divergence of its flux but also due to a source term, $-\rho_0 uw\bar{U}'$, on the right hand side. This source of wave energy arises due to the interaction of the vertical transport of horizontal momentum, $\rho_0 uw$ (often called the Reynolds stress), and the background shear, $\bar{U}'$. Because wave energy is not conserved in time it cannot be used to quantify internal wave transmission in cases with background shear.

A quantity related to wave energy that is conserved is the pseudoenergy, $\mathcal{E}$. Pseudoenergy is defined to be a conserved quantity that is quadratic in the disturbance fields in the small-amplitude limit. In constant stratification and shear the pseudoenergy is given by

$$\mathcal{E} = \frac{1}{2}\rho_0 \left(u^2 + w^2 + N^2\xi^2 - 2\zeta\xi\bar{U} + \zeta\xi^2\bar{U}'\right) \qquad \text{(A.39)}$$

(Scinocca and Shepherd, 1992). We can show that $\mathcal{E}$ is a conserved quantity if it satisfies a relation of the form

$$\frac{\partial \mathcal{E}}{\partial t} + \boldsymbol{\nabla} \cdot \boldsymbol{F} = 0, \qquad \text{(A.40)}$$

where $\boldsymbol{F}$ is the flux of pseudoenergy. This is done by adding the product of the vorticity equation (A.13a) and $\rho_0 \left(\frac{1}{2}\bar{U}'\xi - \bar{U}\right)\xi$ and the product of equation (A.13b) and $\rho_0 \left(\bar{U}'\xi - \bar{U}\right)\zeta$ to the energy equation (A.38). The resulting equation is

$$\frac{\partial \mathcal{E}}{\partial t} + \frac{\partial F_x}{\partial x} + \frac{\partial F_z}{\partial z} = 0 \qquad \text{(A.41)}$$

where F_x is the horizontal flux of pseudoenergy given by

$$F_x = u\left(p + \mathcal{E}\right) + \bar{U}\left(E - \rho_0 w^2 + \mathcal{E}\right) - \frac{1}{6}\rho_0 N^2 \bar{U}'\xi^3 \qquad \text{(A.42a)}$$

and F_z is the vertical flux of pseudoenergy given by

$$F_z = w\left(p + \rho_0 u\bar{U} + \mathcal{E}\right). \qquad \text{(A.42b)}$$

Averaging over a period and keeping only the leading order components in the small amplitude limit these properties simplify to

$$\langle \mathcal{E} \rangle = \frac{1}{2}\rho_0 \left(\langle u^2 \rangle + \langle w^2 \rangle + N^2 \langle \xi^2 \rangle - 2 \langle \zeta \xi \rangle \bar{U} \right) \tag{A.43a}$$

$$\langle F_x \rangle = \langle up \rangle + \bar{U} \left(\langle E \rangle - \rho_0 \langle w^2 \rangle + \langle \mathcal{E} \rangle \right) \tag{A.43b}$$

$$\langle F_z \rangle = \langle wp \rangle + \rho_0 \langle uw \rangle \bar{U}. \tag{A.43c}$$

Pseudoenergy in the small amplitude limit can also be found by calculating the difference between the energy of the total system and the energy of the background, $\frac{1}{2}\rho_0 \bar{U}^2$. The total energy is found by replacing the perturbation velocity, u, in the definition for E with the total horizontal velocity

$$U = \bar{U} + u + \mathcal{M} + \mathcal{O}\left(A_u^3\right). \tag{A.44}$$

Here

$$\mathcal{M} \equiv - \langle \zeta \xi \rangle \tag{A.45}$$

is the second order contribution of internal waves to the total horizontal velocity and is often referred to as the *wave-induced mean-flow*. It is analogous to the Stokes-drift in the case of surface waves. Keeping only the highest order terms after making this substitution we recover (A.43a). The expressions for pseudoenergy and its flux can be further simplified for internal waves in a constant background flow. Applying the polarization relations we find that

$$\langle E \rangle = 2\rho_0 N^2 |A_\xi|^2 \tag{A.46a}$$

$$\langle \mathcal{E} \rangle = \langle E \rangle \frac{\omega}{\Omega} \tag{A.46b}$$

$$\langle F_x \rangle = c_{g_x} \langle \mathcal{E} \rangle \tag{A.46c}$$

$$\langle F_z \rangle = c_{g_z} \langle \mathcal{E} \rangle \tag{A.46d}$$

as expected. Note that in this limit the pseudoenergy is simply the wave action $\mathcal{A} = \frac{\langle E \rangle}{\Omega}$ multiplied by the absolute frequency, ω.

Appendix B

Additional Results

The figures presented here contrast the late time results of simulations for wavepackets with small and finite initial amplitudes. The plots are much the same as the rightmost panels of Figure 3.2 except these waves have vertical wavenumbers of $m = -0.4, -0.7$, and $-1.4\,k$.

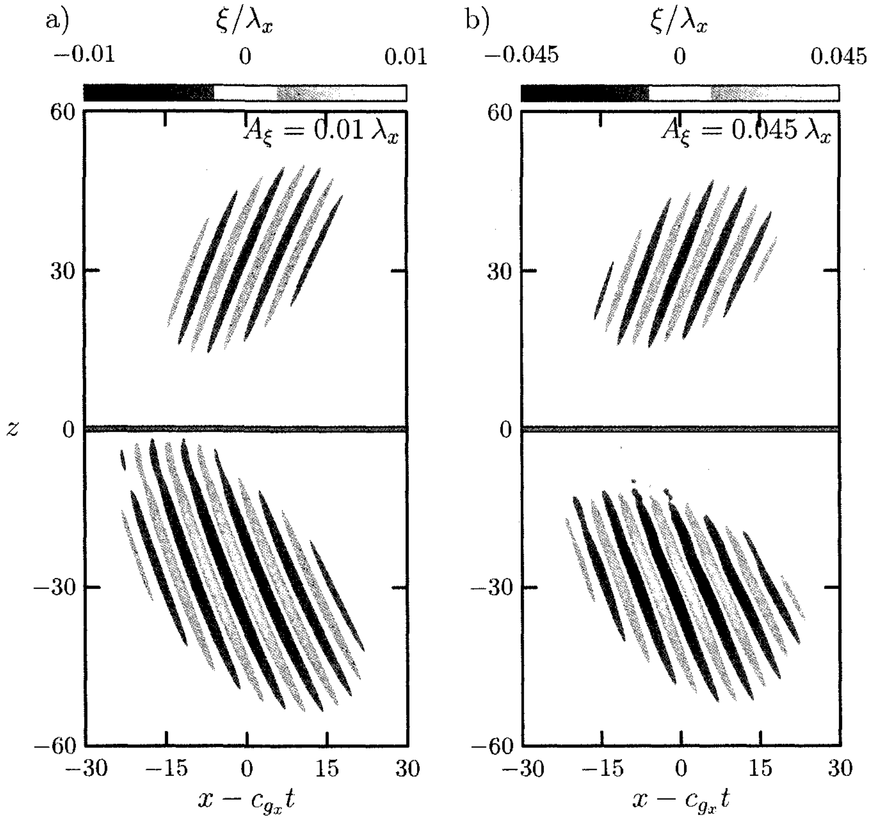

Figure B.1: The normalized vertical displacement field from two fully numerical simulations of horizontally compact wavepackets prescribed initially by (3.2) impinging on a N^2-barrier of width $L = 1\,k^{-1}$ after $t = 190\,N_0^{-1}$. The barrier is depicted by the centre line and the horizontal domain is shifted by c_{g_x} so that wavepackets remain centred. The domain size is in units of k^{-1}. Simulations are initialized with $\sigma_x = \sigma_z = 10\,k^{-1}$, $z_0 = 3\,\sigma_z$, $m = -0.4\,k$, and $A_\xi = 0.01\,\lambda_x$, in a), while $A_\xi = 0.05\,\lambda_x$, in b).

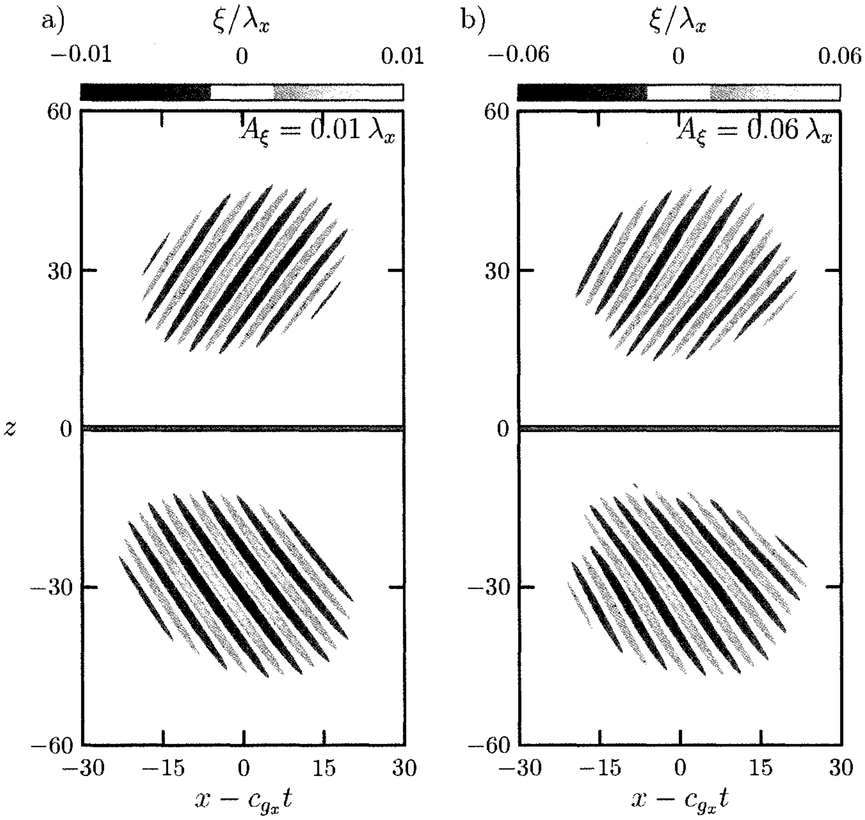

Figure B.2: The normalized vertical displacement field from two fully numerical simulations of horizontally compact wavepackets prescribed initially by (3.2) impinging on a N^2-barrier of width $L = 1\,k^{-1}$ after $t = 155\,N_0^{-1}$. The barrier is depicted by the centre line and the horizontal domain is shifted by c_{g_x} so that wavepackets remain centred. The domain size is in units of k^{-1}. Simulations are initialized with $\sigma_x = \sigma_z = 10\,k^{-1}$, $z_0 = 3\,\sigma_z$, $m = -0.7\,k$, and $A_\xi = 0.01\,\lambda_x$, in a), while $A_\xi = 0.06\,\lambda_x$, in b).

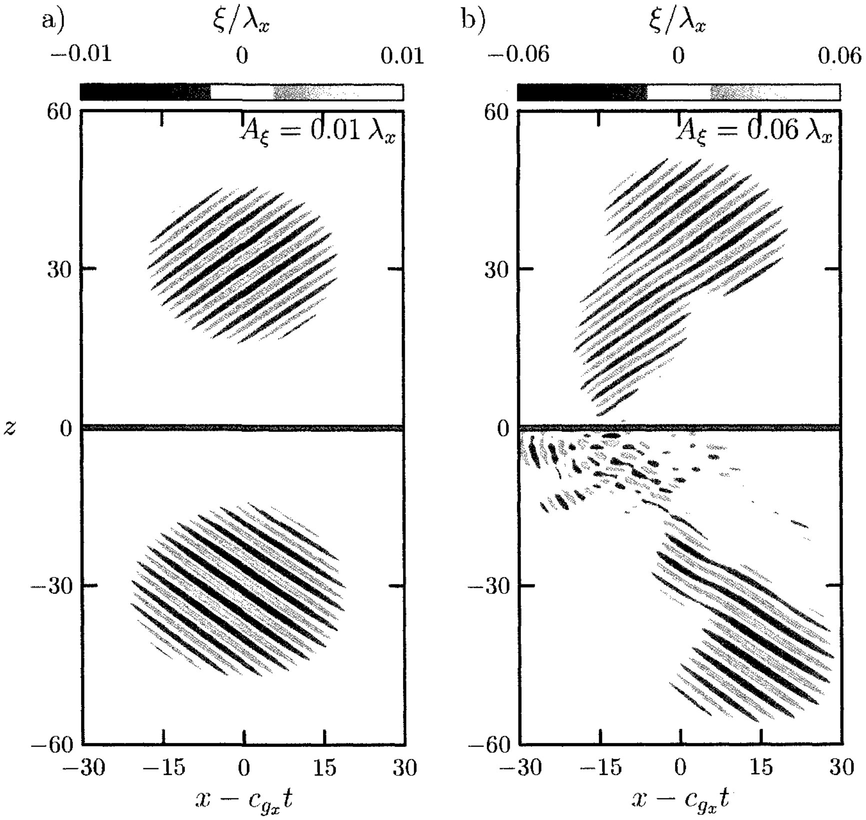

Figure B.3: The normalized vertical displacement field from two fully numerical simulations of horizontally compact wavepackets prescribed initially by (3.2) impinging on a N^2-barrier of width $L = 1\,k^{-1}$ after $t = 220\,N_0^{-1}$. The barrier is depicted by the centre line and the horizontal domain is shifted by c_{g_x} so that wavepackets remain centred. The domain size is in units of k^{-1}. Simulations are initialized with $\sigma_x = \sigma_z = 10\,k^{-1}$, $z_0 = 3\,\sigma_z$, $m = -1.4\,k$, and $A_\xi = 0.01\,\lambda_x$, in a), while $A_\xi = 0.06\,\lambda_x$, in b).